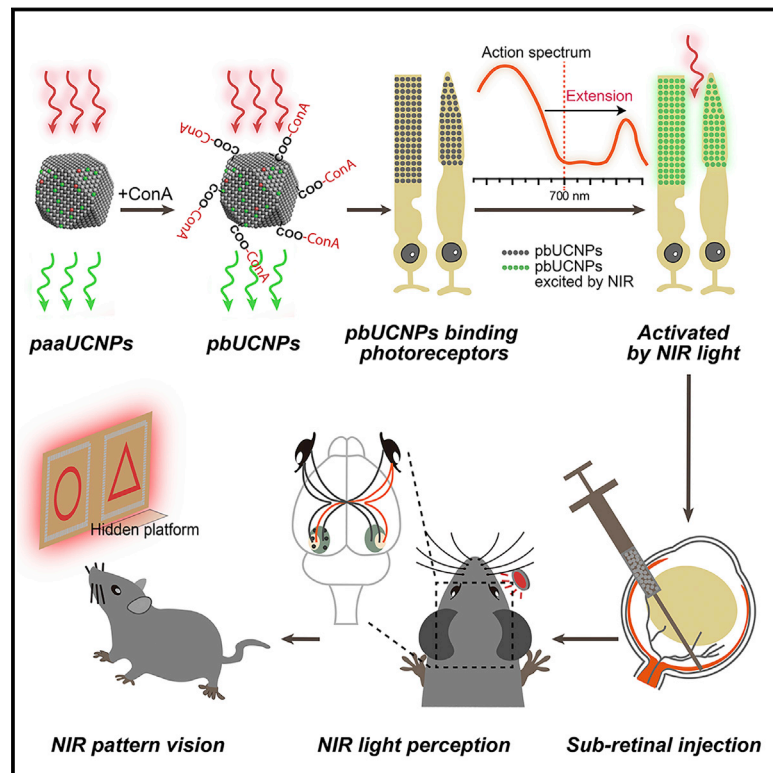


Mammalian Near-Infrared Image Vision through Injectable and Self-Powered Retinal Nanoantennae

Graphical Abstract



Authors

Yuqian Ma, Jin Bao, Yuanwei Zhang, ..., Yang Zhao, Gang Han, Tian Xue

Correspondence

baojin@ustc.edu.cn (J.B.), gang.han@umassmed.edu (G.H.), xuetian@ustc.edu.cn (T.X.)

In Brief

Injectable photoreceptor-binding nanoparticles with the ability to convert photons from low-energy to high-energy forms allow mice to develop infrared vision without compromising their normal vision and associated behavioral responses.

Highlights

- We designed ocular injectable photoreceptor-binding upconversion nanoparticles
- The nanoparticles are safe and enable NIR light sensation and pattern vision
- This NIR pattern vision is compatible with native daylight vision
- This method offers options for mammalian vision repair and enhancement

Mammalian Near-Infrared Image Vision through Injectable and Self-Powered Retinal Nanoantennae

Yuqian Ma,^{1,5} Jin Bao,^{1,2,5,*} Yuanwei Zhang,^{3,5} Zhanjun Li,³ Xiangyu Zhou,¹ Changlin Wan,¹ Ling Huang,³ Yang Zhao,³ Gang Han,^{3,*} and Tian Xue^{1,2,4,6,*}

¹Hefei National Laboratory for Physical Sciences at the Microscale, Neurodegenerative Disorder Research Center, CAS Key Laboratory of Brain Function and Disease, School of Life Sciences, Division of Life Sciences and Medicine, University of Science and Technology of China, Hefei, Anhui 230026, China

²Center for Excellence in Brain Science and Intelligence Technology, Chinese Academy of Sciences, Shanghai 200031, China

³Department of Biochemistry and Molecular Pharmacology, University of Massachusetts Medical School, Worcester, MA 01605, USA

⁴Institute for Stem Cell and Regeneration, Chinese Academy of Sciences, Beijing 100101, China

⁵These authors contributed equally

⁶Lead Contact

*Correspondence: baojin@ustc.edu.cn (J.B.), gang.han@umassmed.edu (G.H.), xuetian@ustc.edu.cn (T.X.)

<https://doi.org/10.1016/j.cell.2019.01.038>

SUMMARY

Mammals cannot see light over 700 nm in wavelength. This limitation is due to the physical thermodynamic properties of the photon-detecting opsins. However, the detection of naturally invisible near-infrared (NIR) light is a desirable ability. To break this limitation, we developed ocular injectable photoreceptor-binding upconversion nanoparticles (pbUCNPs). These nanoparticles anchored on retinal photoreceptors as miniature NIR light transducers to create NIR light image vision with negligible side effects. Based on single-photoreceptor recordings, electroretinograms, cortical recordings, and visual behavioral tests, we demonstrated that mice with these nanoantennae could not only perceive NIR light, but also see NIR light patterns. Excitingly, the injected mice were also able to differentiate sophisticated NIR shape patterns. Moreover, the NIR light pattern vision was ambient-daylight compatible and existed in parallel with native daylight vision. This new method will provide unmatched opportunities for a wide variety of emerging bio-integrated nanodevice designs and applications.

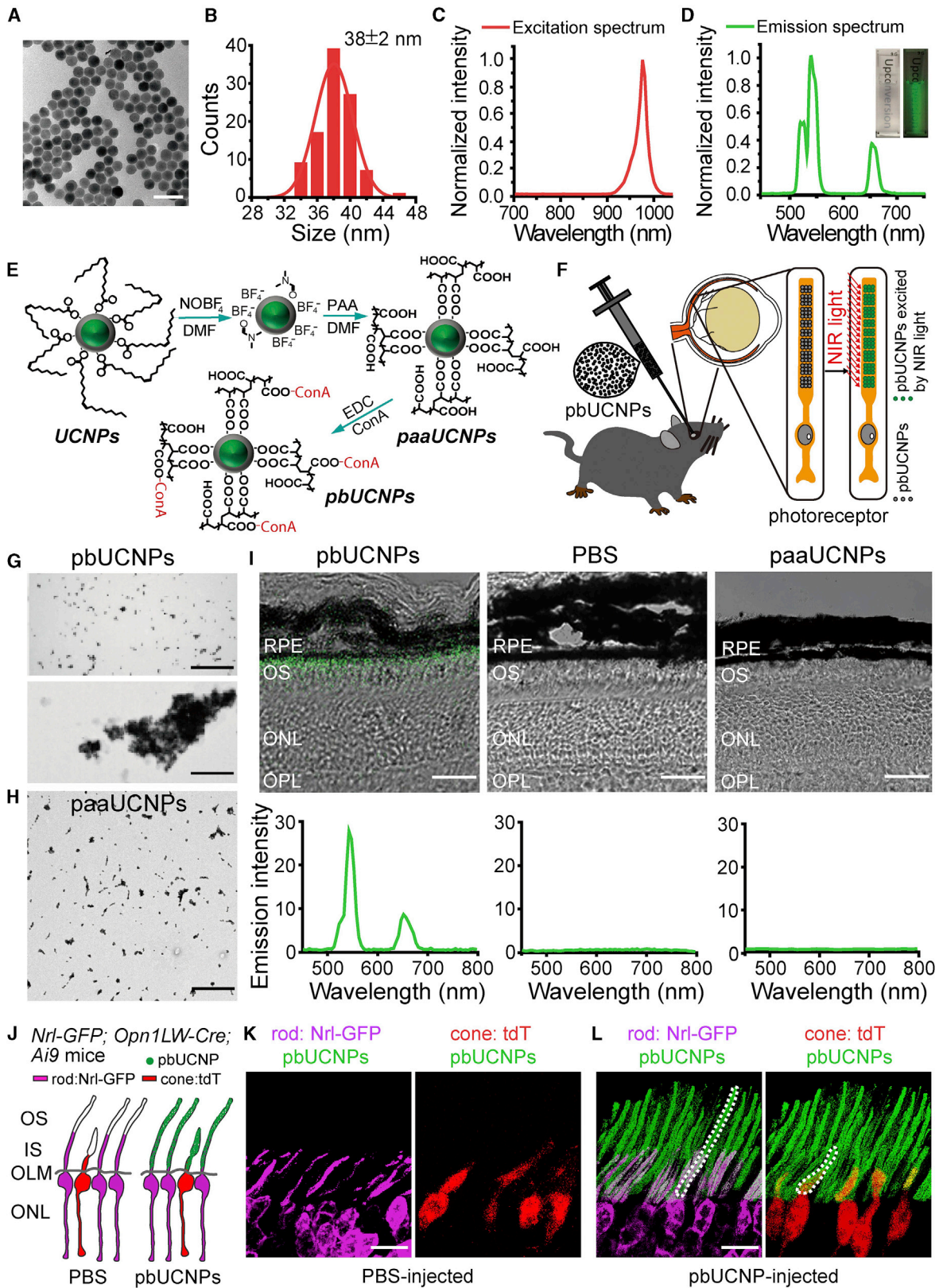
INTRODUCTION

Vision is an essential sensory modality for humans. Our visual system detects light between 400 and 700 nm (Dubois, 2009; Wyszecki and Stiles, 1982; Schnapf et al., 1988), so called visible light. In mammalian photoreceptor cells, light absorbing pigments, consisting of opsins and their covalently linked retinals, are known as intrinsic photon detectors. However, the detection of longer wavelength light, such as near-infrared (NIR) light, though a desirable ability, is a formidable challenge for mammals. This is because detecting longer wavelength light, with

lower energy photons, requires opsins (e.g., human red cone opsins) to have much lower energy barriers. Consequently, this results in unendurable high thermal noise, thus making NIR visual pigments impractical (Ala-Laurila et al., 2003; Baylor et al., 1980; Luo et al., 2011; St George, 1952). This physical limitation means that no mammalian photoreceptor can effectively detect NIR light that exceeds 700 nm, and mammals are unable to see NIR light and to project a NIR image to the brain.

To this end, the successful integration of nanoparticles with biological systems has accelerated basic scientific discoveries and their translation into biomedical applications (Desai, 2012; Mitragotri et al., 2015). To develop abilities that do not exist naturally, miniature nanoscale devices and sensors designed to intimately interface with mammals including humans are of growing interest. Here, we report on an ocular injectable, self-powered, built-in NIR light nanoantenna that can extend the mammalian visual spectrum to the NIR range. These retinal photoreceptor-binding upconversion nanoparticles (pbUCNPs) act as miniature energy transducers that can transform mammalian invisible NIR light *in vivo* into short wavelength visible emissions (Liu et al., 2017; Wu et al., 2009). As sub-retinal injections are a commonly used ophthalmological practice in animals and humans (Hauswirth et al., 2008; Peng et al., 2017), our pbUCNPs were dissolved in PBS and then injected into the sub-retinal space in the eyes of mice. These nanoparticles were then anchored and bound to the photoreceptors in the mouse retina.

Through *in vivo* electroretinograms (ERGs) and visually evoked potential (VEP) recordings in the visual cortex, we showed that the retina and visual cortex of the pbUCNP-injected mice were both activated by NIR light. From animal behavioral tests, we further demonstrated that the pbUCNP-injected mice acquired NIR light sensation and unique ambient daylight-compatible NIR light image vision. As a result, the built-in NIR nanoantennae allowed the mammalian visual spectrum to extend into the NIR realm effectively without obvious side effects. Excitingly, we found that pbUCNP-injected animals perceived both NIR and visible light patterns simultaneously. They also differentiated between sophisticated NIR light shape patterns (such as triangles



(legend on next page)

and circles). Importantly, this nanoscale device activated the photoreceptors by an exceptionally low power NIR light-emitting diode (LED) light (1.62 mW/cm^2), which was attributed to the proximity between the nanoantennae and photoreceptors in the eye. Moreover, we comprehensively examined the biocompatibility of the pbUCNPs and found negligible side effects.

Therefore, these novel photoreceptor-binding NIR light nanoantennae provide an injectable, self-powered, biocompatible, and NIR-visible light compatible solution to extend the mammalian visual spectrum into the NIR range. This concept-proving research should guide future studies with respect to extending human and non-human vision without the need for any external device or genetic manipulation. Endowing mammals with NIR vision capacity could also pave the way for critical civilian and military applications.

RESULTS

The Design of pbUCNPs

The human eye is most sensitive to visible light at an electromagnetic wavelength of $\sim 550 \text{ nm}$ under photopic conditions (Bieber et al., 1995; Boynton, 1996). To convert NIR light to this wavelength, we generated core-shell-structured upconversion nanoparticles (UCNPs) (i.e., $38 \pm 2 \text{ nm}$ $\beta\text{-NaYF}_4\text{:20\%Yb, 2\%Er@}\beta\text{-NaYF}_4$) (Figures 1A and 1B), which exhibited an excitation spectrum peak at 980 nm and emission peak at 535 nm upon 980-nm light irradiation (Mai et al., 2006; Wu et al., 2015) (Figures 1C and 1D). To design water-soluble pbUCNPs, we further conjugated concanavalin A protein (ConA) with poly acrylic acid-coated UCNPs (paaUCNPs) (Figure 1E; STAR Methods). ConA can bind to sugar residue and derivatives of the photoreceptor outer segment, forming glycosidic bonds (Bridges, 1981; Bridges and Fong, 1980; Rutishauser and Sachs, 1975). Successful ConA conjugation on the surface of the UCNPs was suggested by the appearance of N-H bending peaks in the Fourier transform infrared (FT-IR) spectrum (Figure S1A) and by the $\sim 285 \text{ nm}$ protein absorption on the ultraviolet-visible spectroscopy (UV/Vis)

spectrum (Figure S1B). To confirm the glycosidic bonds between ConA and glycoproteins, we added β -cyclodextrin, which possesses a similar glucosyl unit as that found on the photoreceptor outer segment, to the pbUCNP solution. Characteristic ConA- β -cyclodextrin aggregation thus occurred, as seen in the transmission electron microscope (TEM) images (Figure 1G) and dynamic light scattering (DLS) spectrum (Figure S1C). This result suggests that the pbUCNPs can bind to glycoproteins on the photoreceptor outer segment. In contrast, the paaUCNPs without ConA remained monodispersed when β -cyclodextrin was added (Figures 1H and S1D). After injecting these pbUCNPs into the mouse sub-retinal spaces (Figures 1F and S1E), we observed that, through the glycosidic bond, these pbUCNPs self-anchored and remained tightly bound to the inner and outer segments of both rods and cones (Figures 1J–1L) forming a layer of built-in nanoantennae with the characteristic upconversion spectrum (Figures 1I, left, S1F, and S1G). In contrast, the injected paaUCNPs were loosely bound and easily removed from the photoreceptors with gentle washing (Figure 1I, right).

We then evaluated the biocompatibility and potential side effects of the pbUCNPs *in vivo*. We found that the pbUCNP injection did not cause a higher rate of adverse reactions compared with the control PBS injection. All common minor or transient side effects (e.g., cataracts, corneal opacity) generally associated with sub-retinal injection (Qi et al., 2015; Zhao et al., 2011) disappeared completely 2 weeks after the injections (Table S1). In addition, we evaluated possible retinal degeneration by counting the number of photoreceptors in the retinal outer nuclear layer (ONL), a standard and widely used method in the field of retinal research, as photoreceptors are sensitive and prone to degenerate upon stress (Chen et al., 2006; Namekata et al., 2013; Wang et al., 2013). As a result, we observed that the retinal layer structure and the number of photoreceptor layers in the retinal ONL were not changed, even with $50 \mu\text{g}$ of pbUCNPs injected into each eye, up to 2 months after the injections (Figures 2A and 2B). This result clearly suggested that there was no obvious retinal degeneration using this standard measure.

Figure 1. Characterizations of pbUCNPs

- (A) Transmission electron microscopy (TEM) image of UCNPs (as-synthesized core-shell-structured $\beta\text{-NaYF}_4\text{:20\%Yb, 2\%Er@}\beta\text{-NaYF}_4$). Scale bar, 100 nm .
- (B) Corresponding size distribution of UCNPs.
- (C) Excitation spectrum of UCNPs measured as emission light intensity at 535 nm by $700\text{--}1,040 \text{ nm}$ excitation.
- (D) Emission spectrum of UCNPs upon 980-nm continuous wave (CW) laser irradiation. Inset displays photographs of UCNP solutions with (right) and without (left) 980-nm CW laser excitation.
- (E) Schematic illustration of surface modification procedures for ConA-functionalized photoreceptor-binding UCNPs (pbUCNPs).
- (F) Left: illustration of sub-retinal injection of pbUCNPs in mice. See also Figure S1. Right: illustration of pbUCNPs binding to the outer segments of photoreceptors and generation of green light upon near-infrared (NIR) light illumination.
- (G) TEM images of pbUCNPs before (top) and after (bottom) addition of 200 nM β -cyclodextrin showing characteristic aggregation of pbUCNPs in the presence of β -cyclodextrin. See also Figure S1. Scale bar, $2 \mu\text{m}$.
- (H) TEM images of UCNPs without ConA-conjugation (paaUCNPs) mixed with 200 nM β -cyclodextrin, showing no obvious aggregation. See also Figure S1. Scale bar, $2 \mu\text{m}$.
- (I) Top: overlays of transmission and luminescence optical images (green: 980-nm excitation/ 535-nm emission) of retinal slices from pbUCNP-injected, PBS-injected, and paaUCNP-injected mice. Bottom: emission spectrum recorded from retinal outer segment layers (OS) upon 980-nm light excitation. All retinal slices were washed with PBS during fixation. Only pbUCNPs remained bound to the photoreceptor outer segments. RPE, retinal pigment epithelium; OS, outer segment of photoreceptors; ONL, outer nuclear layer; OPL, outer plexiform layer. Scale bar, $30 \mu\text{m}$.
- (J) Schematic illustration of distribution of pbUCNPs (green) in the retina. Rods are labeled with Nrl-GFP in pseudo color violet. Cones are labeled with Opn1LW-Cre; Ai9-*Isl*-tdTomato in pseudo color red. OS, outer segment of photoreceptors; IS, inner segment of photoreceptors; OLM, outer limiting membrane; ONL, outer nuclear layer.
- (K and L) Overlaid green (pbUCNPs)/violet (rods) and green (pbUCNPs)/red (cones) channel fluorescence images of retina from PBS-injected mice (K) and pbUCNP-injected mice (L). Examples of continuous inner and outer segments of a rod and a cone are shown in dashed contour lines. Scale bars, $10 \mu\text{m}$.

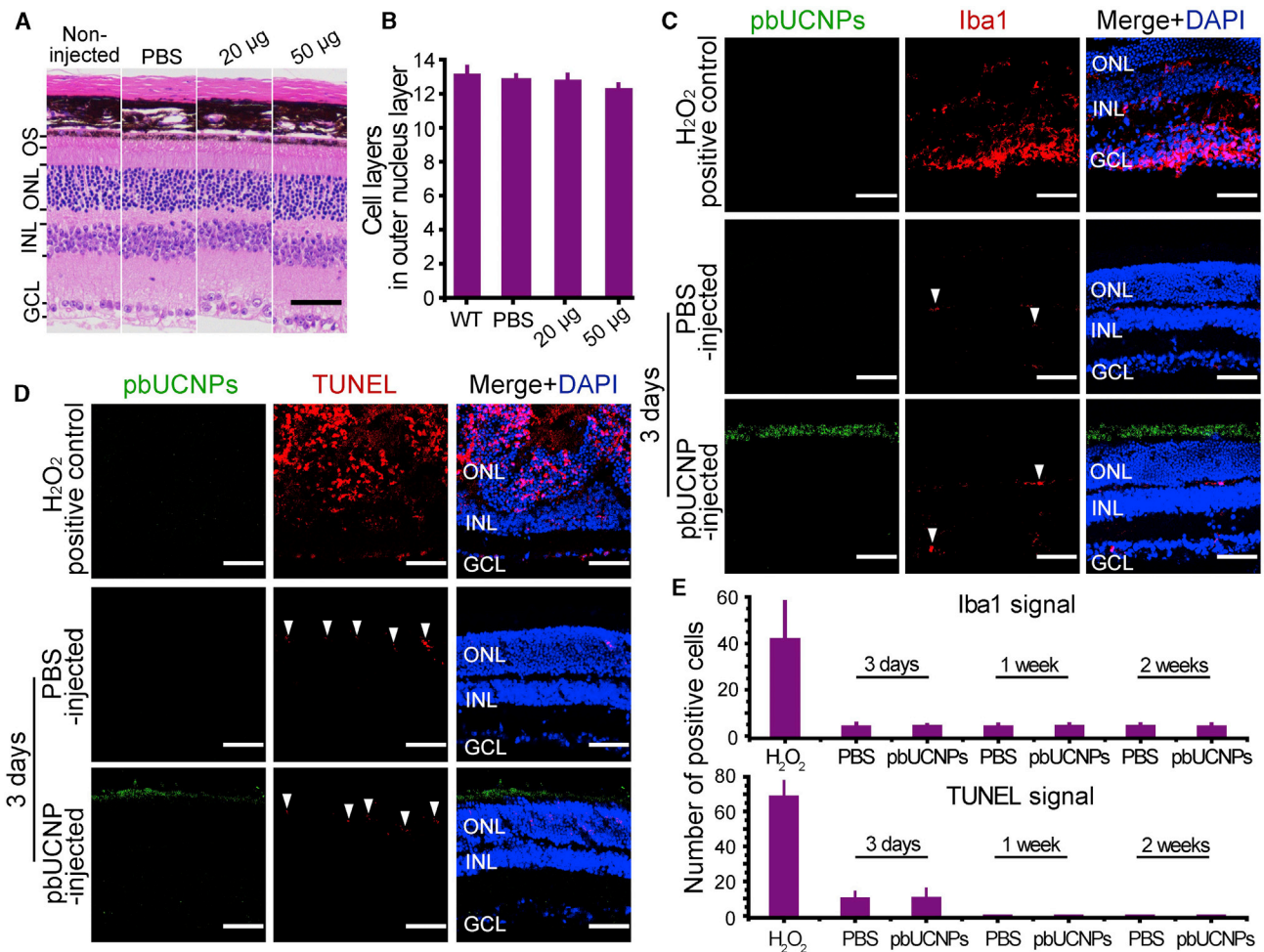


Figure 2. Biocompatibility of pbUCNPs

(A) H&E staining of retinal slices from non-injected, PBS-injected, 20 μ g/eye and 50 μ g/eye pbUCNP-injected mice. OS, outer segment of photoreceptors; ONL, outer nuclear layer; INL, inner nuclear layer; GCL, ganglion cell layer. Scale bar, 50 μ m.
 (B) Number of cell layers in outer nuclear layer (ONL) of retinae. Data are mean \pm SD (n = 4 retinae).
 (C) Microglia marker Iba1 staining of retinal slices 3 days after injection. H₂O₂-injected mice (positive control) showed strong activation of microglia. Few basal Iba1 signals were observed in the pbUCNP-injected retina, similar to that observed in PBS-injected retina (indicated by arrow heads). Red, Iba1; green, pbUCNP emission upon excitation by NIR light; blue, DAPI (4',6-diamidino-2-phenylindole) signal indicating cell nuclei. Scale bar, 50 μ m.
 (D) Apoptosis detection by TUNEL staining 3 days after injection. Strong TUNEL signals were observed in the H₂O₂-injected mouse retinae (positive control), but few were observed in PBS-injected or pbUCNP-injected mice (indicated by arrow heads). Red, TUNEL staining; green, pbUCNP emission upon excitation by NIR light; blue, DAPI. Scale bar, 50 μ m.
 (E) Number of Iba1 and TUNEL stained cells per 0.04 mm² averaged from four retinae for each condition. See also Figure S2. Data are mean \pm SD (n = 4 retinae). See also Table S1.

Moreover, we examined potential inflammation in the retinal through microglia marker Iba1 staining that is a widely used indicator of microglia accumulation (Kradly et al., 2005). From this, we observed negligible retinal inflammation at 3 days or 1, 2, 4, and 10 weeks after pbUCNP injection (Figures 2C, 2E, and S2A). We further examined retinal cell apoptosis after injection via terminal deoxynucleotidyl transferase deoxyuridine triphosphate (dUTP) nick-end labeling (TUNEL). We only found sparse TUNEL signals 3 days after injection in both the PBS and pbUCNP-injected retinae (Figure 2D), with the TUNEL signals being undetectable 1, 2, 4, and 10 weeks after pbUCNP injection (Figures 2E and S2B). These results suggest that the pbUCNP

injection did not cause obvious acute or long-term side effects. In addition, the excitation and emission spectra of the pbUCNPs in either fixed or fresh retinae were in good agreement with those measured from pbUCNP solution, indicating that binding with the photoreceptors did not change the characteristics of the pbUCNPs (Figures S2C and S2D).

NIR Light-Mediated Photoreceptor Activation

Based on the biocompatibility noted above, we tested if the photoreceptors could be activated by NIR light with the help of pbUCNPs. We performed single rod suction pipette recordings on acutely dissected retinae from pbUCNP-injected and

non-injected mice (Figure 3A). The action spectra of rods from pbUCNP-injected and non-injected mice were identical in the visible light range, with differences only appearing after 900 nm, where the action spectra of rods from pbUCNP-injected mice matched the excitation spectra of pbUCNPs (Figure S3A). The rods from pbUCNP-injected mice had normal visible light (535 nm)-elicited photocurrents compared with that of non-injected mice (Figures 3B and 3D). The 980-nm light flash elicited rod photocurrents from pbUCNP-injected mice (Figure 3E), whereas the rods from non-injected mice exhibited no responses (Figure 3C). The amplitude and kinetics of the 980-nm light-elicited photocurrents were identical to those activated by 535-nm visible light (Figures 3F–3H). The similar time-to-peak values suggest that, compared to the visible light stimulation, there was no delay in the activation of the rods by NIR light. Furthermore, the pbUCNPs did not alter the light adaptation or dark noise characteristics of the rods, and rods adapted to visible and NIR light in the same manner following the Weber-Fechner relationship (Baylor et al., 1980; Morshedian et al., 2018; Fu et al., 2008) (Figure S4). To determine whether the pbUCNPs can serve as NIR nanosensors *in vivo*, we recorded the population response of photoreceptors activated by light via ERGs (Dalke et al., 2004) (Figure 3I). Upon 980-nm NIR light illumination to the eye, the ERG from pbUCNP-injected mice resembled that of visible light-induced responses, whereas no such signal could be detected from the non-injected control mice. Furthermore, we performed ERG recordings on pbUCNP-injected rod-functionless mice (*Gnat1*^{-/-}) and demonstrated that, through the pbUCNPs, 980-nm NIR light indeed activated cones *in vivo* (Figure S3B).

NIR Light Sensation of pbUCNP-Injected Mice

To reveal whether pbUCNP-injected mice could see NIR light, we first performed pupillary light reflex (PLR) experiments (Xue et al., 2011). The pupils of the pbUCNP-injected mice showed strong constrictions upon 980-nm light illumination, whereas the non-injected control mice did not exhibit PLR with the same NIR illumination (Figure 4A). Moreover, we discovered that the PLR of the pbUCNP-injected mice was two orders of magnitude more sensitive to NIR light than that of the non-photoreceptor-binding paaUCNP-injected mice (Figure 4B). This was attributed to the proximity between the pbUCNPs and the bound photoreceptors. Photon upconversion was measured (Figure S5A) and showed a non-linear light intensity relationship plotted at the log-log scale (Figure S5B). We fitted the power relationship between emitted 535-nm light and 980-nm excitation light and determined the power to be 1.6. Interestingly, we found that this non-linearity was also shown in the NIR light-induced behavior. The light dose-response curves of the PLR (normalized pupil area versus light intensity) were fitted to the Hill function. The NIR light-induced PLR dose-response curve was steeper than that of visible light, and the Hill coefficients for the NIR and visible light PLR dose-responses were 1.10 and 0.78, respectively (Figure S5C). To obtain the theoretical NIR light PLR dose-response curve, the fitted upconversion function was applied to the visible light PLR dose-response Hill function. This theoretical NIR light PLR dose-response curve

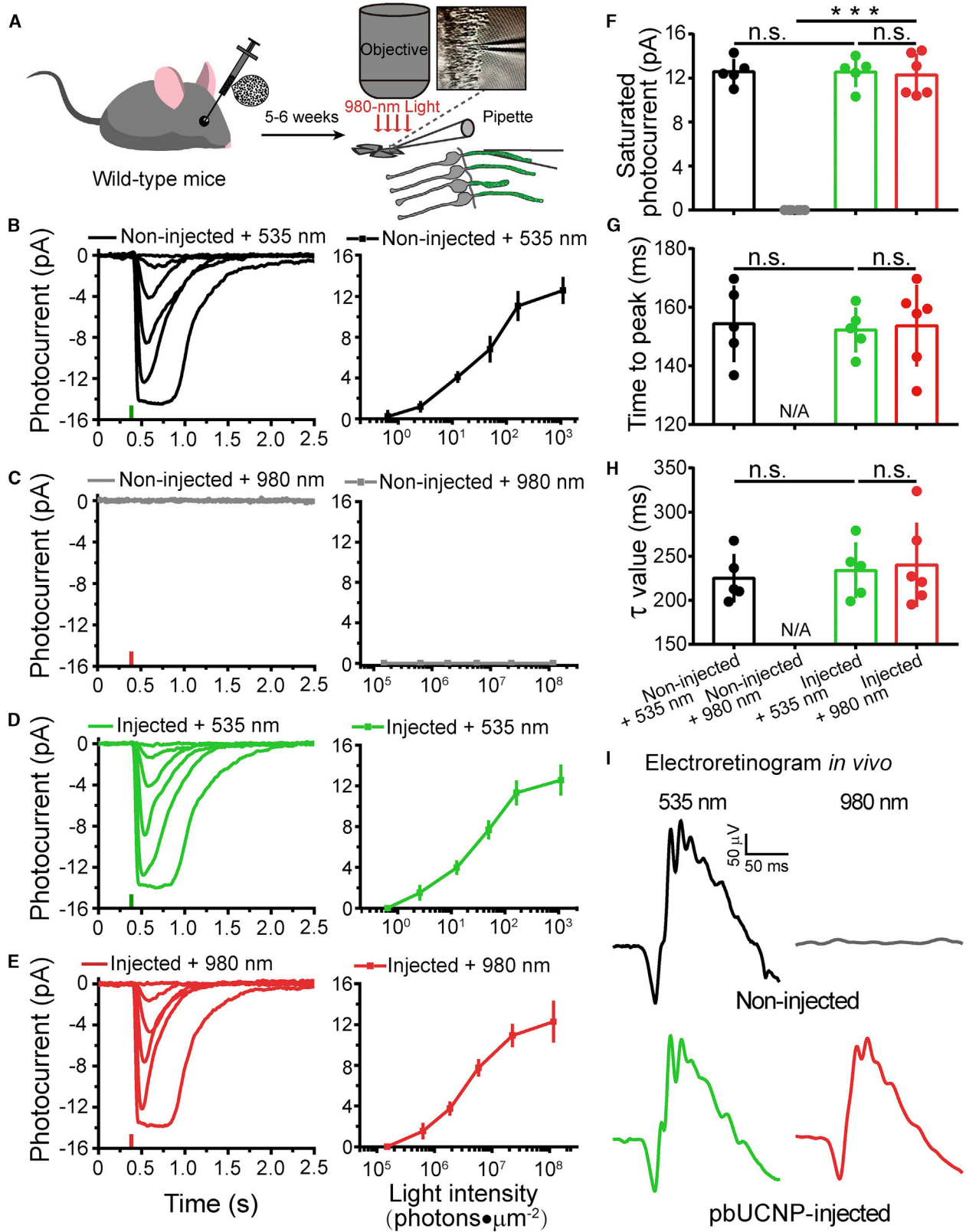
agreed well with the experimental NIR light PLR response (Figure S5C). Therefore, the non-linearity shown in the NIR light-induced behavior was attributed to the non-linearity of the upconversion process.

In addition to the above sub-conscious light sensation PLR behavior, we also explored whether pbUCNP-injected mice could consciously perceive NIR light. In this regard, we performed light-dark box experiments with visible and NIR light (Figures 4C and 4D) as well as light-induced fear-conditioning experiments (Figures 4E and 4F). In the conventional light-dark box experiments with visible light, mice instinctively preferred the dark box to the light box illuminated with visible light. In our study, we replaced conventionally used visible light with 980-nm LED light, which delivered 8.1×10^7 photons $\times \mu\text{m}^{-2} \times \text{s}^{-1}$ at the center of the light box, equal to a power density of 1.62 mW/cm². The pbUCNP-injected mice exhibited a significant preference for the dark box, whereas the non-injected control mice could not distinguish between the NIR light (980 nm)-illuminated and dark boxes (Figure 4D; Video S1). This suggests that mice with injected nanoantennae perceived NIR light and exhibited innate light-sensing behavior. To exclude the possibility of any visible light emission from the NIR LEDs, the emission spectra of the 980-nm LEDs were measured and no light emission below 900 nm was detected (Figures S5D and S5E).

We then tested whether such NIR light perception can serve as a visual cue for learned behavior. Mice were trained to pair a 20-s 535-nm light pulse to a 2-s foot shock (Figure 4E) in order to acquire a conditioned freezing behavior. After acquisition of such conditioning, mice received either NIR light at 980 nm or visible light at 535 nm as conditional stimuli (CS) in the test trials. The pbUCNP-injected mice showed significant freezing behavior in response to both wavelengths, whereas the non-injected control mice exhibited freezing behavior only to visible light stimuli (Figure 4F; Video S2). These results clearly demonstrated that mice acquired NIR light sensation and were able to “see” NIR light with our ocular injectable photoreceptor targeting nanoantennae.

NIR Light-Activated Imaging Visual Pathway of pbUCNP-Injected Mice

In addition to the NIR light sensation, we were curious whether pbUCNP-injected mice had acquired NIR light image visual ability. In general, visual image perception is associated with activation of the visual cortex. In order to record visually evoked potential (VEPs), we placed recording electrodes in six different locations of the visual cortex (No. 1, 2, 3, and 5 in the monocular areas and No. 4 and 6 in the binocular areas) during contralateral eye illumination (Cooke et al., 2015; Smith and Trachtenberg, 2007) (Figure 5A). When the visible 535-nm light pulse was applied, VEPs were detected at all locations in both the non-injected controls and pbUCNP-injected mice (Figures 5B and 5D). In contrast, under 980-nm NIR light illumination, no VEPs were observed in the control mice, but were detected from the binocular visual cortical areas in pbUCNP-injected mice (Figures 5C and 5E). This is topologically consistent with the pbUCNP injection site (temporal side, binocular projection area) in the retina.



(legend on next page)

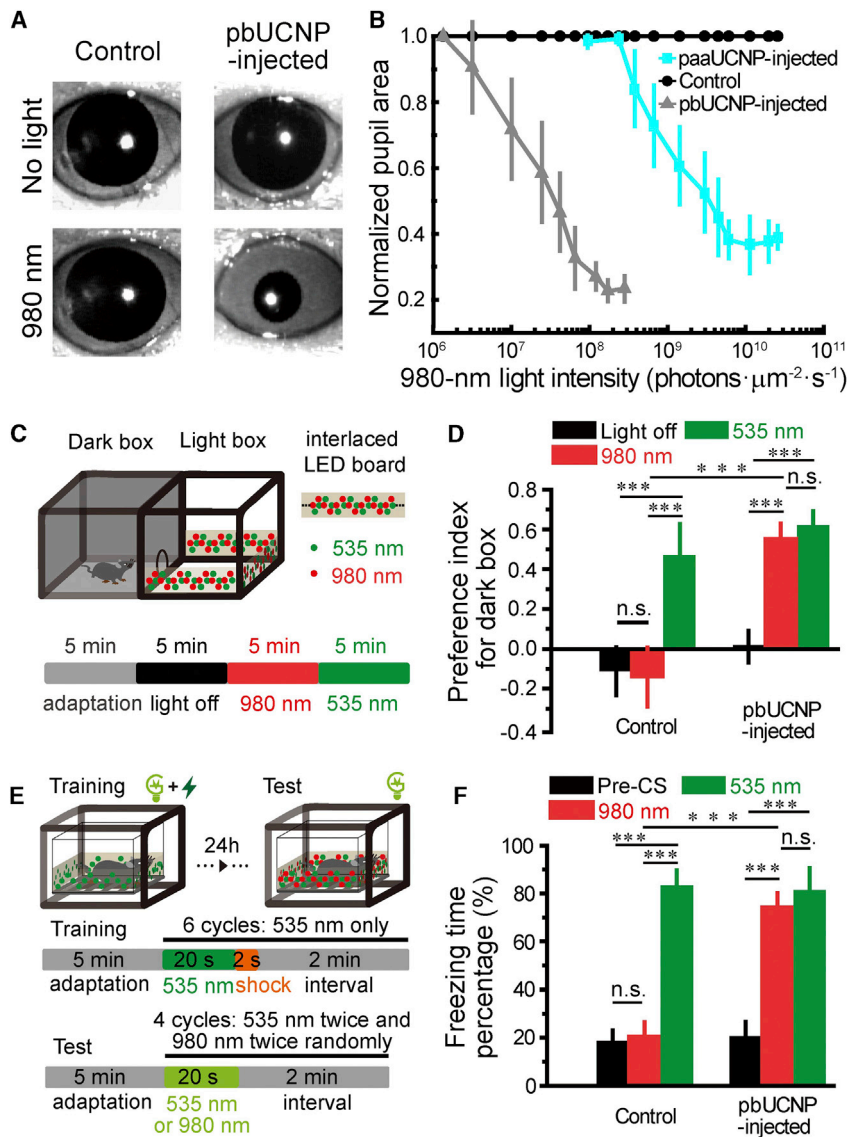


Figure 4. NIR Light Sensation of pbUCNP-Injected Mice

(A) Images showing pupil constriction from non-injected control and pbUCNP-injected mice under 980-nm light stimulation (40 s). Intensity of 980-nm light: 1.21×10^8 photons $\times \mu\text{m}^{-2} \times \text{s}^{-1}$.

(B) Dose-response curves of normalized pupil constriction with 980-nm light stimulation (paaUCNP-injected mice, $n = 4$; pbUCNP-injected mice, $n = 5$; control mice, $n = 4$; data are mean \pm SD).

(C) Light-dark box experiment diagram. Light box was illuminated with an array of LED lights interlaced by 980-nm and 535-nm LEDs. Illumination protocol is shown at the bottom. Each section contained four episodes and each episode was 5 min long. The first 5-min episode was adaptation in the light-dark box with ambient light followed by a 5-min episode in complete darkness. The 980-nm and 535-nm LEDs were then lit consecutively for the light box for 5 min each.

(D) Preference index for dark box under three different light box conditions (light off, 980 nm, and 535 nm). Preference index = (time spent in dark box - in light box) / (time spent in dark box + in light box). Intensities of the 980-nm and 535-nm lights at the center of the box were 8.1×10^7 and 9.1×10^2 photons $\times \mu\text{m}^{-2} \times \text{s}^{-1}$, respectively (Control: $n = 5$, pbUCNP-injected: $n = 6$; data are mean \pm SD, two-sided t test, $***p < 0.001$; n.s., not significant).

(E) Fear-conditioning experiment diagram and protocol. A 535-nm light pulse was paired with a foot-shock to form conditioning during training. Tests were then carried out 24 h later with a 980-nm or 535-nm light pulse alone.

(F) Percentages of freezing time during 20 s “Pre-CS,” 980-nm, and 535-nm light stimulation (“Pre-CS”: before conditional stimulation, a 20-s period of adaptation right before light stimulation onset). Intensities of the 980-nm and 535-nm lights at the center of the box were 1.07×10^8 and 1.47×10^3 photons $\times \mu\text{m}^{-2} \times \text{s}^{-1}$, respectively. Data are mean \pm SD (control: $n = 6$, pbUCNP-injected: $n = 7$; two-sided t test; n.s., not significant; $***p < 0.001$).

See also [Figure S5](#) and [Videos S1](#) and [S2](#).

NIR Light Pattern Vision

We next examined whether mice obtained NIR light pattern vision. Accordingly, Y-shaped water maze behavioral experiments were conducted to determine whether mice could

discriminate between different light patterns (Prusky et al., 2000) (Figure 6A). The mice were trained to find a hidden platform that was associated with one of two patterns. We designed five different tasks to examine their NIR pattern vision ability

Figure 3. NIR Light-Mediated Photoreceptor Activation through pbUCNPs

(A) Illustration of rod outer segment suction pipette recordings from freshly isolated retinæ. Stimulation light was either 980-nm or 535-nm through the imaging objective.

(B–E) Photocurrents and intensity-response curves of rods from non-injected mice with 535-nm (B) ($n = 5$) or 980-nm (C) ($n = 6$) light stimulations and pbUCNP-injected mice with 535-nm (D) ($n = 5$) or 980-nm (E) ($n = 6$) light stimulations. Tiny colored vertical bars on the x axis indicate time of light flashes. Photocurrent traces were averaged from 5–7 sweeps. Intensity-response data are mean \pm SD.

(F) Saturated photocurrent in (B)–(E).

(G) Time-to-peak, time from light stimulation to peak amplitude of dim light photocurrents in (B)–(E).

(H) Decay time constant of dim light photocurrent in (B)–(E). Data are mean \pm SD; n.s., not significant; $***p < 0.001$.

(I) Electroretinograms (ERGs) recorded from mice under 535-nm or 980-nm light stimulation. No response was observed in non-injected control mice under 980-nm light stimulation (gray). Light intensities: 535 nm, 8.26×10^3 photons $\times \mu\text{m}^{-2}$; 980 nm, 9.83×10^8 photons $\times \mu\text{m}^{-2}$.

See also [Figures S3](#) and [S4](#).

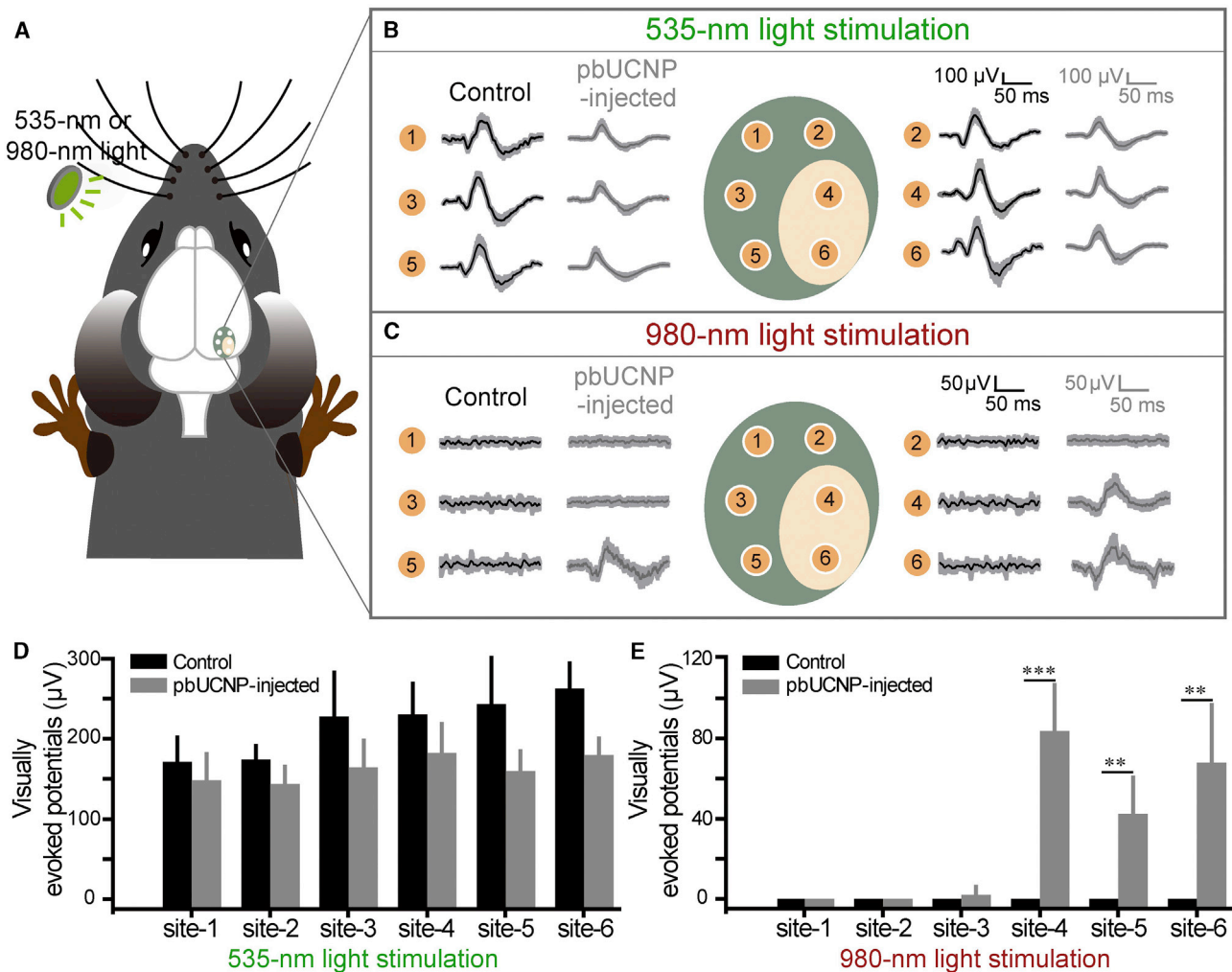


Figure 5. NIR Light Activated the Imaging Visual Pathway of pbUCNP-Injected Mice

(A) Diagram of six recording sites for visually evoked potentials (VEPs) in the mouse visual cortex.

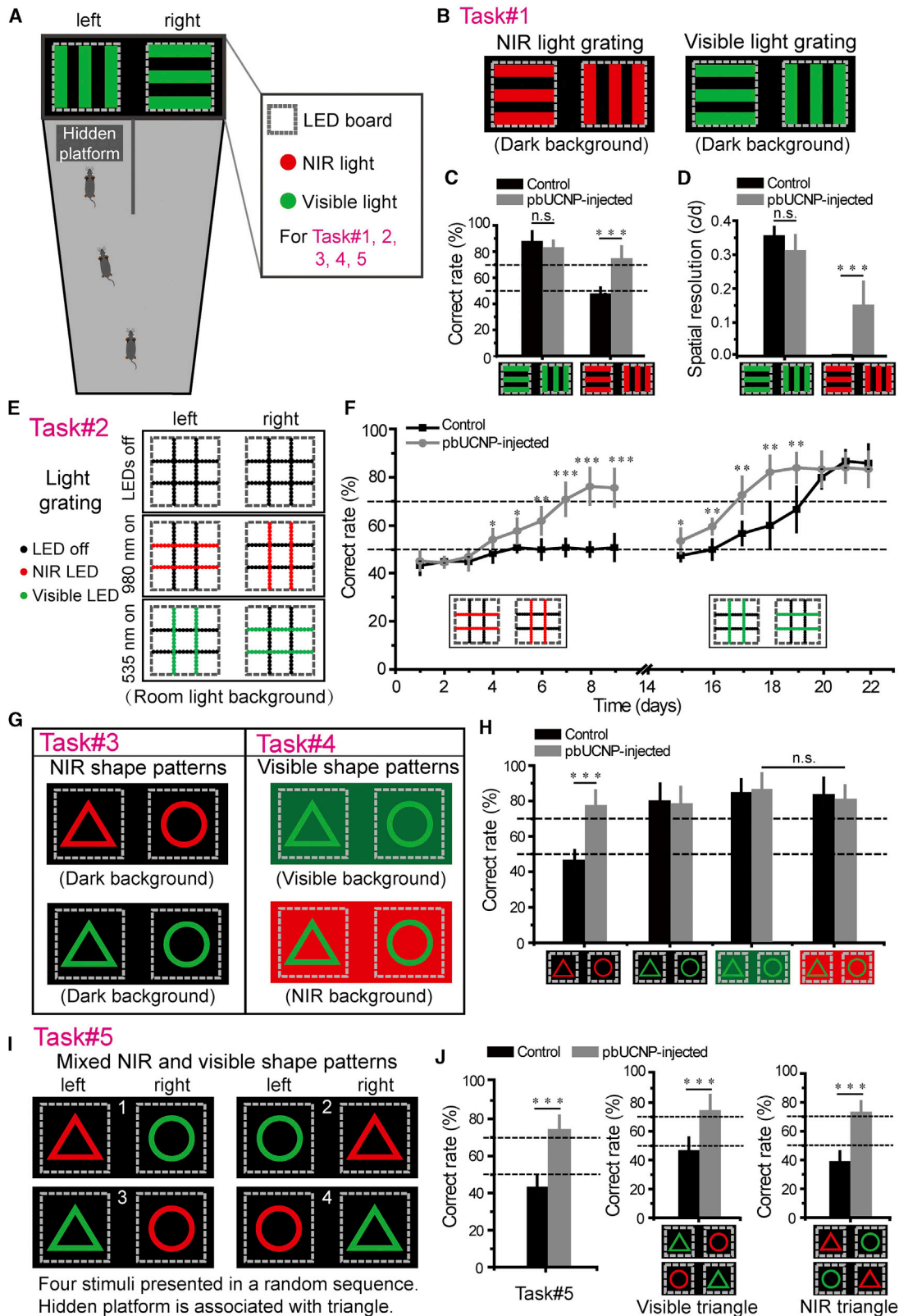
(B and C) VEPs of non-injected control (black traces) and pbUCNP-injected mice (gray traces) under 535-nm (B) and 980-nm (C) light illumination. Intensities of the 535-nm and 980-nm lights were 3.37×10^3 and 7.07×10^8 photons $\times \mu\text{m}^{-2} \times \text{s}^{-1}$, respectively. Recording sites 1, 2, 3, and 5 were monocular areas; 4 and 6 were binocular areas. Traces were averaged from six sweeps and presented as mean \pm SD (shaded area).

(D and E) Peak VEPs triggered by 535-nm (D) or 980-nm (E) light at each recording site (mean \pm SD, $n = 4$ for both, two-sided t test, ** $p < 0.01$, *** $p < 0.001$).

regarding different pattern stimuli and various background light conditions. Task 1 used light gratings as pattern stimuli (Figures 6B and S6A). After training with 980-nm light gratings, the pbUCNP-injected mice were able to discriminate between the two orientations (vertical or horizontal) of the NIR light gratings, whereas the non-injected control mice made such choices in a random manner (Figure 6C; Video S3). In the parallel control testing, when the mice were trained and tested with visible light gratings, both the pbUCNP-injected and non-injected mice were able to find the associated platform (Figures 6C, S6B, and S6C). We then measured the spatial resolution of the NIR image perception. The pbUCNP-injected mice detected the visible light gratings with a maximum spatial frequency of 0.31 ± 0.04 cycles/degree, which did not significantly differ from that of the non-injected control mice (0.35 ± 0.02 cycles/degree). This indicates

that the sub-retinal injection of pbUCNPs did not interfere with visible light vision. With respect to NIR light gratings, the pbUCNP-injected mice detected a maximum of 0.14 ± 0.06 cycles/degree. This decrease in spatial resolution in NIR light vision may be due to the isotropic radiation and scattering of the *in situ* transduced visible light from the NIR light-excited pbUCNPs (Figures 6D and S6D).

In addition, to confirm if visible light background interfered with the NIR light pattern perception, we designed Task 2 using two LED boards with visible (535 nm) and NIR (980 nm) LED arrays arranged in a perpendicular manner on each board. These two boards appeared identical under an ambient visible light background when all LEDs (visible and NIR) were turned off. The orientations for the 535-nm and 980-nm LED stripes between the two boards were 90° rotated respectively (Figure 6E).



(legend on next page)

Trainings were carried out under visible room light (196 lux) and with only the 980-nm LEDs on. In the tests, only pbUCNP-injected mice learnt to locate the platform (Figure 6F), indicating that NIR light pattern vision persisted in the visible light-illuminated environment. Interestingly, we subsequently tested these mice with the 535-nm LEDs on and 980-nm LEDs off. Both pbUCNP-injected and control mice could discriminate the visible light gratings, again indicating that pbUCNP injection did not affect normal visible light vision. Additionally, pbUCNP-injected mice could discriminate the visible light gratings from the beginning of the test, suggesting that pbUCNP-injected mice were able to implement the rule learnt from the NIR light pattern to visible light pattern discrimination, indicating that NIR light patterns did not differ perceptually from visible light patterns for pbUCNP-injected mice (Figure 6F; Video S4).

To test more sophisticated pattern vision, we further prompted animals to discriminate triangular and circular patterns in Task 3 (Figure 6G). We found that pbUCNP-injected mice were able to discriminate NIR and visible light patterns in the dark environment, whereas non-injected control mice could only detect the visible light pattern (Figures 6H, S6E, and S6F; Video S5), indicating that pbUCNP-injected mice could perceive sophisticated NIR light patterns. We subsequently speculated whether background NIR light would interfere with the visible light pattern vision of pbUCNP-injected mice. Thus, in Task 4, mice were tested to discriminate between visible light triangles and circles under a visible or NIR light background (Figure 6G). Same as control mice, the pbUCNP-injected mice did not behave differently regarding their ability to discriminate visible light patterns under dark, visible, or NIR light backgrounds (Figures 6H and S6F–S6H; Video S5). These results clearly suggest that background NIR light does not interfere with visible light pattern perception.

Task 5 was designed to test whether pbUCNP-injected mice could see NIR and visible light patterns simultaneously. In general, saturation by visible light is a common problem for conventionally used tools, such as optoelectronic night vision devices or IR cameras, as it prevents smooth detection between visible and NIR light objects. To test if our built-in NIR light vision could overcome this problem and coexist with visible light vision, we designed the following experiments. Mice were first trained in a Y-shaped water maze with visible light triangles and circles to learn that the platform was associated with triangles only. During

the test trials, we presented one visible (535 nm) and one NIR (980 nm) light in a triangular-circular pattern at the left-right ends of the water maze, shuffled in a random sequence (Figure 6I). Only the pbUCNP-injected mice were able to discriminate between the two patterns with different shapes and wavelengths (Figures 6J, left, and S6I). To exclude the possibility that mice simply used either visible or NIR light patterns to guide decision-making rather than seeing them simultaneously, we calculated the correct choice rates separately for the visible and NIR light triangle patterns. In the subset of stimuli where the triangular patterns was in visible light (Figure 6J, middle), control mice selected both sides randomly, indicating they did not simply use the visible triangle to make decisions. When the circular pattern was in visible light, control mice still picked the side randomly, indicating that the mice did not use the strategy of avoiding circles to make decisions (Figure 6J, right). In contrast, pbUCNP-injected mice made correct choices in both cases (Video S5), suggesting they used visible and NIR light patterns together to guide behavior. These results clearly indicate that the built-in nanoantennae enabled mice to see visible and NIR light patterns simultaneously.

DISCUSSION

In this study, we demonstrated the successful application of UCNPs as ocular injectable NIR light transducers, which extended mammalian vision into the NIR realm. These implanted nanoantennae were proven to be biocompatible and did not interfere with normal visible light vision. Importantly, animals were able to detect NIR and visible light images simultaneously.

Extension of the Visual Spectrum into the NIR Range

One way to obtain NIR light vision is to implement new machinery for NIR photon transduction, such as the thermal detection of snakes (Gracheva et al., 2010). However, a more plausible method to achieve such NIR photon detection is the use of the endogenous visual system. The method we developed here utilized the very first step of the visual image perception process through photoreceptor outer-segment binding NIR nanoantennae. The NIR light image was projected to the retina through the optical part of the eyes, cornea, and lens, after which the pbUCNPs upconverted NIR light into visible light and then activated the bound photoreceptors. Subsequently, the retinal

Figure 6. NIR Light Pattern Vision of pbUCNP-Injected Mice

- (A) Diagram of Y-shaped water maze for Tasks 1–5.
(B) Stimuli of Task 1. Experiments were under dark background. See also Figure S6.
(C) Correct rates of Task 1 for light grating discrimination (pbUCNP-injected mice: n = 7; non-injected control mice: n = 6).
(D) Visual spatial resolutions of pbUCNP-injected and control mice for 535-nm and 980-nm light gratings.
(E) Diagram of visual stimuli in Task 2. Light grating stimulations were LED arrays with ambient room light as background.
(F) Correct rates of Task 2 with respect to discrimination of 980-nm (days 1–9) and 535-nm (days 15–22) light LED gratings under room light background (pbUCNP-injected mice: n = 7 and control mice: n = 5).
(G) Visual stimuli of Tasks 3 and 4. Triangular and circular patterns were made of LEDs and presented at the end of the water maze.
(H) Correct rates of Tasks 3 and 4 in discriminating triangular and circular patterns under dark, visible light, or NIR light background (pbUCNP-injected: n = 5 and control: n = 6).
(I) Diagram of four stimuli in Task 5. Four stimuli were mixed and shuffled randomly in position.
(J) Correct rates of Task 5 in discriminating NIR and visible light shape patterns simultaneously (left), with triangular pattern in visible light (middle) and in NIR light (right) (pbUCNP-injected: n = 5 and Control: n = 6). All data are mean \pm SD (two-sided t test, **p < 0.01, ***p < 0.001; n.s., not significant). See also Videos S3, S4, and S5.

circuit and cortical visual system generated perception of the NIR image. It is important to note that these injected nanoantennae did not interfere with natural visible light vision. The ability to simultaneously detect visible and NIR light patterns suggests enhanced mammalian visual performance by extending the native visual spectrum without genetic modification and avoiding the need for bulky external devices. This approach offers several advantages over the currently used optoelectronic devices, such as no need for any external energy supply, and is compatible with other human activities.

Improved Efficiency through ConA Modification of UCNP

Regarding the practical applications of UCNP, higher visual sensitivity and resolution are desirable. We modified the UCNP and generated photoreceptor-binding nanoparticles to increase the proximity between the nanoparticles and photoreceptors. Thus, sensitivity to NIR light with respect to generating light-induced behaviors was improved by two orders of magnitude. Therefore, it is now possible to use biocompatible low-power NIR LEDs to elicit visual behavior in animals, rather than the more invasive high-power NIR lasers inevitably used in conventional UCNP biomedical applications (Chen et al., 2018; He et al., 2015). In the Y-shaped water maze experiment, we estimated that the 980-nm LED light was transduced to 535-nm light by the pbUCNPs at 293 photons \times μm^{-2} \times s^{-1} intensity at the retina. The rod and cone-mediated visual behavior thresholds of mice are 0.012 and 200 photons \times μm^{-2} \times s^{-1} at the cornea, respectively (Sampath et al., 2005), equal to 0.003 and 50 photons \times μm^{-2} \times s^{-1} at the retina (Do et al., 2009). Therefore, in our system, the 293 photons \times μm^{-2} \times s^{-1} at the retina was adequate to activate both rod and cone photoreceptors, and in practice, this NIR visual system was able to detect NIR light that was of several magnitudes lower intensity than currently applied. Compared to rods, cones encode several orders of magnitude higher intensity light and are more important for human high acuity vision. Thus, pbUCNP-bound cones may mediate high-resolution NIR image pattern vision. Retinae also possess intrinsic photosensitive retinal ganglion cells (ipRGCs), which mediate non-image forming visual functions, such as photoentrainment of the circadian rhythm (Do and Yau, 2010). Under the intensity used in our behavioral experiment, NIR light did not activate ipRGCs (Figure S5F), which was likely due to the longer distance of ipRGCs to pbUCNPs and their low sensitivity (Do et al., 2009). With respect to NIR image spatial resolution, pbUCNP-injected mice had good NIR eye sight (0.14 ± 0.06 cycles/degree, half of the visible image resolution), allowing them to see sophisticated NIR light patterns.

Biocompatible NIR Nanoantennae

Sub-retinal injection in humans is a common practice in ophthalmological treatment (Hauswirth et al., 2008; Peng et al., 2017). The implantation of microscale sub-retinal devices is a potential method of repairing vision following retinal photoreceptor degeneration, though current devices can lead to biocompatibility issues, such as retinal detachment, fibrosis, and inflammation (Zrenner, 2013). Yet, this did not occur in our system, as the intimate contact between the pbUCNPs and photoreceptors did

not cause any separation between the photoreceptors and retinal pigment epithelium, the latter of which is the supporting layer for photoreceptors. As a result, neither inflammation nor apoptosis occurred, which is in line with that of another reported retinal application of rare earth nanoparticles (Chen et al., 2006). The stability and compatibility of the pbUCNPs were also demonstrated by successful detection of NIR light images, even after 10 weeks without any repeated injections.

Further Development of pbUCNPs

In the present study, we created NIR light vision while overcoming several key drawbacks that yet exist in currently used man-made systems. It may also be possible to design NIR color vision through multicolor NIR light-sensitive UCNP that have multiple NIR light absorption peak wavelengths and corresponding multicolor visible light emissions. Further applications using our strategy for visual repair and enhancement could also be achieved by similar nanoparticles with tailored light absorptions. In addition, combined with a drug delivery system, these photoreceptor-binding nanoparticles could be modified to release small molecules locally upon light stimulation.

In summary, these nanoparticles not only provide the potential for close integration within the human body to extend the visual spectrum, but also open new opportunities to explore a wide variety of animal vision-related behaviors. Furthermore, they exhibit considerable potential with respect to the development of bio-integrated nanodevices in civilian encryption, security, military operations, and human-machine interfaces, which require NIR light image detection that goes beyond the normal functions of mammals, including human beings. Moreover, in addition to visual ability enhancement, this nanodevice can serve as an integrated and light-controlled system in medicine, which could be useful in the repair of visual function as well as in drug delivery for ocular diseases.

STAR★METHODS

Detailed methods are provided in the online version of this paper and include the following:

- KEY RESOURCES TABLE
- CONTACT FOR REAGENT AND RESOURCE SHARING
- EXPERIMENTAL MODEL AND SUBJECT DETAILS
 - Mice
- METHOD DETAILS
 - Synthesis of pbUCNPs
 - Sub-retinal injection
 - Distribution and spectrum analysis
 - Retinal histology
 - TUNEL Apoptosis detection
 - Microglia staining
 - Single cell electrophysiology
 - Electroretinography
 - Pupillary light reflex
 - Light-dark box
 - Light induced fear conditioning
 - Visually evoked potential
 - Y shaped water maze

● QUANTIFICATION AND STATISTICAL ANALYSIS

- Imaging quantifications
- Statistics
- Fitting procedures

SUPPLEMENTAL INFORMATION

Supplemental Information can be found with this article online at <https://doi.org/10.1016/j.cell.2019.01.038>.

A video abstract is available at <https://doi.org/10.1016/j.cell.2019.01.038#mmc7>.

ACKNOWLEDGMENTS

We thank members of the Neuroscience Pioneer Club for valuable discussions. We thank Drs. Dangsheng Li and Zilong Qiu for reading this manuscript and providing helpful comments. We thank Dr. Yang Xiang from University of Massachusetts Medical School for helpful discussion. We thank Min Wei and Shouzhen Li for helpful discussions and Jiawei Shen and Dr. Huan Zhao for helping illustration drawing and videos clipping. We thank Dr. Kai Huang and Mr. Nuo Yu for helping characterizing nanoparticles. We thank Dr. Qiuping Wang and Xiaokang Ding from National Synchrotron Radiation Laboratory for helping with the measurement of various spectra of light sources. We thank Dr. Yuen Wu and Xing Wang from School of Chemistry and Materials Science (USTC) for helping with the measurement of the absorption spectrum of pbUCNPs. We acknowledge support from the National Key Research and Development Program of China (2016YFA0400900), the Strategic Priority Research Program of the Chinese Academy of Science (XDA16020603, XDPB10, XDB02010000), the National Young Scientists 973 Program of China (2013CB967700), the National Natural Science Foundation of China (81790644, 61890953, 31322024, 81371066, 91432104, 31571073, 81401025, 61727811, 91748212), the NIH (R01MH103133 to G.H.), a UMass OTCV award, a Worcester Foundation Mel Cutler Award to G.H., and the Human Frontier Science Program (RGY-0090/2014).

AUTHOR CONTRIBUTIONS

Conceptualization, T.X. and G.H.; Methodology, Y.M., J.B., G.H., and T.X.; Investigation, Y.M., J.B., Y. Zhang, Z.L., L.H., Y. Zhao, X.Z., C.W., G.H., and T.X.; Validation, J.B., G.H., and T.X.; Formal Analysis, Y.M. and J.B.; Writing – Original Draft, J.B., Y.M., Y. Zhang, G.H., and T.X.; Writing – Review & Editing, J.B., Y.M., G.H., and T.X.; Funding Acquisition, J.B., G.H., and T.X.; Supervision, J.B., G.H., and T.X.

DECLARATION OF INTERESTS

T.X. and G.H. have a patent application related to this work.

Received: June 6, 2018

Revised: November 9, 2018

Accepted: January 24, 2019

Published: February 28, 2019

REFERENCES

Ala-Laurila, P., Albert, R.J., Saarinen, P., Koskelainen, A., and Donner, K. (2003). The thermal contribution to photoactivation in A2 visual pigments studied by temperature effects on spectral properties. *Vis. Neurosci.* *20*, 411–419.

Baylor, D.A., Matthews, G., and Yau, K.W. (1980). Two components of electrical dark noise in toad retinal rod outer segments. *J. Physiol.* *309*, 591–621.

Bieber, M.L., Volbrecht, V.J., and Werner, J.S. (1995). Spectral efficiency measured by heterochromatic flicker photometry is similar in human infants and adults. *Vision Res.* *35*, 1385–1392.

Bourin, M., and Hascoët, M. (2003). The mouse light/dark box test. *Eur. J. Pharmacol.* *463*, 55–65.

Boynton, R.M. (1996). Frederic Ives Medal paper. History and current status of a physiologically based system of photometry and colorimetry. *J. Opt. Soc. Am. A Opt. Image Sci. Vis.* *13*, 1609–1621.

Bridges, C.D.B. (1981). Lectin receptors of rods and cones. Visualization by fluorescent label. *Invest. Ophthalmol. Vis. Sci.* *20*, 8–16.

Bridges, C.D.B., and Fong, S.L. (1980). Lectin receptors on rod and cone membranes. *Photochem. Photobiol.* *32*, 481–486.

Burstyn-Cohen, T., Lew, E.D., Través, P.G., Burrola, P.G., Hash, J.C., and Lemke, G. (2012). Genetic dissection of TAM receptor-ligand interaction in retinal pigment epithelial cell phagocytosis. *Neuron* *76*, 1123–1132.

Calvert, P.D., Krasnoperova, N.V., Lyubarsky, A.L., Isayama, T., Nicoló, M., Kosaras, B., Wong, G., Gannon, K.S., Margolskee, R.F., Sidman, R.L., et al. (2000). Phototransduction in transgenic mice after targeted deletion of the rod transducin alpha -subunit. *Proc. Natl. Acad. Sci. USA* *97*, 13913–13918.

Chen, J., Patil, S., Seal, S., and McGinnis, J.F. (2006). Rare earth nanoparticles prevent retinal degeneration induced by intracellular peroxides. *Nat. Nanotechnol.* *1*, 142–150.

Chen, S., Weitemier, A.Z., Zeng, X., He, L., Wang, X., Tao, Y., Huang, A.J.Y., Hashimoto, Y., Kano, M., Iwasaki, H., et al. (2018). Near-infrared deep brain stimulation via upconversion nanoparticle-mediated optogenetics. *Science* *359*, 679–684.

Cooke, S.F., and Bear, M.F. (2013). How the mechanisms of long-term synaptic potentiation and depression serve experience-dependent plasticity in primary visual cortex. *Philos. Trans. R. Soc. Lond. B Biol. Sci.* *369*, 20130284.

Cooke, S.F., Komorowski, R.W., Kaplan, E.S., Gavornik, J.P., and Bear, M.F. (2015). Erratum: Visual recognition memory, manifested as long-term habituation, requires synaptic plasticity in V1. *Nat. Neurosci.* *18*, 926.

Cui, Z.Z., Feng, R.B., Jacobs, S., Duan, Y.H., Wang, H.M., Cao, X.H., and Tsien, J.Z. (2013). Increased NR2A:NR2B ratio compresses long-term depression range and constrains long-term memory. *Sci. Rep.* *3*, 1036.

Dalke, C., Löster, J., Fuchs, H., Gailus-Durner, V., Soewarto, D., Favor, J., Neuhaus-Klaus, A., Pretsch, W., Gekeler, F., Shinoda, K., et al. (2004). Electroretinography as a screening method for mutations causing retinal dysfunction in mice. *Invest. Ophthalmol. Vis. Sci.* *45*, 601–609.

Desai, N. (2012). Challenges in development of nanoparticle-based therapeutics. *AAPS J.* *14*, 282–295.

Do, M.T.H., and Yau, K.W. (2010). Intrinsically photosensitive retinal ganglion cells. *Physiol. Rev.* *90*, 1547–1581.

Do, M.T., Kang, S.H., Xue, T., Zhong, H., Liao, H.W., Bergles, D.E., and Yau, K.W. (2009). Photon capture and signalling by melanopsin retinal ganglion cells. *Nature* *457*, 281–287.

Dong, A., Ye, X., Chen, J., Kang, Y., Gordon, T., Kikkawa, J.M., and Murray, C.B. (2011). A generalized ligand-exchange strategy enabling sequential surface functionalization of colloidal nanocrystals. *J. Am. Chem. Soc.* *133*, 998–1006.

Dubois, E. (2009). The Structure and Properties of Color Spaces and the Representation of Color Images (Morgan & Claypool Publishers).

Fu, Y., Kefalov, V., Luo, D.G., Xue, T., and Yau, K.W. (2008). Quantal noise from human red cone pigment. *Nat. Neurosci.* *11*, 565–571.

Govardovskii, V.I., Fyhrquist, N., Reuter, T., Kuzmin, D.G., and Donner, K. (2000). In search of the visual pigment template. *Vis. Neurosci.* *17*, 509–528.

Gracheva, E.O., Ingolia, N.T., Kelly, Y.M., Cordero-Morales, J.F., Holloper, G., Chesler, A.T., Sánchez, E.E., Perez, J.C., Weissman, J.S., and Julius, D. (2010). Molecular basis of infrared detection by snakes. *Nature* *464*, 1006–1011.

Hauswirth, W.W., Aleman, T.S., Kaushal, S., Cideciyan, A.V., Schwartz, S.B., Wang, L., Conlon, T.J., Boye, S.L., Flotte, T.R., Byrne, B.J., and Jacobson, S.G. (2008). Treatment of leber congenital amaurosis due to RPE65 mutations by ocular subretinal injection of adeno-associated virus gene vector: short-term results of a phase I trial. *Hum. Gene Ther.* *19*, 979–990.

- He, S., Krippes, K., Ritz, S., Chen, Z., Best, A., Butt, H.J., Mailänder, V., and Wu, S. (2015). Ultralow-intensity near-infrared light induces drug delivery by upconverting nanoparticles. *Chem. Commun. (Camb.)* 51, 431–434.
- Karnas, D., Hicks, D., Mordel, J., Pévet, P., and Meissl, H. (2013). Intrinsic photosensitive retinal ganglion cells in the diurnal rodent, *Arvicanthis ansorgei*. *PLoS ONE* 8, e73343.
- Krady, J.K., Basu, A., Allen, C.M., Xu, Y., LaNoue, K.F., Gardner, T.W., and Levison, S.W. (2005). Minocycline reduces proinflammatory cytokine expression, microglial activation, and caspase-3 activation in a rodent model of diabetic retinopathy. *Diabetes* 54, 1559–1565.
- Le, Y.Z., Ash, J.D., Al-Ubaidi, M.R., Chen, Y., Ma, J.X., and Anderson, R.E. (2004). Targeted expression of Cre recombinase to cone photoreceptors in transgenic mice. *Mol. Vis.* 10, 1011–1018.
- Liu, Y., Lu, Y., Yang, X., Zheng, X., Wen, S., Wang, F., Vidal, X., Zhao, J., Liu, D., Zhou, Z., et al. (2017). Amplified stimulated emission in upconversion nanoparticles for super-resolution nanoscopy. *Nature* 543, 229–233.
- Luo, D.G., Yue, W.W.S., Ala-Laurila, P., and Yau, K.W. (2011). Activation of visual pigments by light and heat. *Science* 332, 1307–1312.
- Mai, H.X., Zhang, Y.W., Si, R., Yan, Z.G., Sun, L.D., You, L.P., and Yan, C.H. (2006). High-quality sodium rare-earth fluoride nanocrystals: controlled synthesis and optical properties. *J. Am. Chem. Soc.* 128, 6426–6436.
- Mitragotri, S., Anderson, D.G., Chen, X., Chow, E.K., Ho, D., Kabanov, A.V., Karp, J.M., Kataoka, K., Mirkin, C.A., Petrosko, S.H., et al. (2015). Accelerating the translation of nanomaterials in biomedicine. *ACS Nano* 9, 6644–6654.
- Morshedian, A., Woodruff, M.L., and Fain, G.L. (2018). Role of recoverin in rod photoreceptor light adaptation. *J. Physiol* 596, 1513–1526.
- Namekata, K., Kimura, A., Kawamura, K., Guo, X., Harada, C., Tanaka, K., and Harada, T. (2013). Dock3 attenuates neural cell death due to NMDA neurotoxicity and oxidative stress in a mouse model of normal tension glaucoma. *Cell Death Differ.* 20, 1250–1256.
- Peng, Y., Tang, L., and Zhou, Y. (2017). Subretinal injection: a review on the novel route of therapeutic delivery for vitreoretinal diseases. *Ophthalmic Res.* 58, 217–226.
- Pittler, S.J., and Baehr, W. (1991). Identification of a nonsense mutation in the rod photoreceptor cGMP phosphodiesterase beta-subunit gene of the rd mouse. *Proc. Natl. Acad. Sci. USA* 88, 8322–8326.
- Prusky, G.T., West, P.W.R., and Douglas, R.M. (2000). Behavioral assessment of visual acuity in mice and rats. *Vision Res.* 40, 2201–2209.
- Qi, Y., Dai, X., Zhang, H., He, Y., Zhang, Y., Han, J., Zhu, P., Zhang, Y., Zheng, Q., Li, X., et al. (2015). Trans-corneal subretinal injection in mice and its effect on the function and morphology of the retina. *PLoS ONE* 10, e0136523.
- Roberts, J.E. (1961). Lanthanum and neodymium salts of trifluoroacetic acid. *J. Am. Chem. Soc.* 83, 1087–1088.
- Rutishauser, U., and Sachs, L. (1975). Cell-to-cell binding induced by different lectins. *J. Cell Biol.* 65, 247–257.
- Sampath, A.P., Strissel, K.J., Elias, R., Arshavsky, V.Y., McGinnis, J.F., Chen, J., Kawamura, S., Rieke, F., and Hurley, J.B. (2005). Recoverin improves rod-mediated vision by enhancing signal transmission in the mouse retina. *Neuron* 46, 413–420.
- Schmidt, T.M., and Kofuji, P. (2010). Differential cone pathway influence on intrinsically photosensitive retinal ganglion cell subtypes. *J. Neurosci.* 30, 16262–16271.
- Schnapf, J.L., Kraft, T.W., Nunn, B.J., and Baylor, D.A. (1988). Spectral sensitivity of primate photoreceptors. *Vis. Neurosci.* 1, 255–261.
- Smith, S.L., and Trachtenberg, J.T. (2007). Experience-dependent binocular competition in the visual cortex begins at eye opening. *Nat. Neurosci.* 10, 370–375.
- Soucy, E., Wang, Y., Nirenberg, S., Nathans, J., and Meister, M. (1998). A novel signaling pathway from rod photoreceptors to ganglion cells in mammalian retina. *Neuron* 21, 481–493.
- St George, R.C.C. (1952). The interplay of light and heat in bleaching rhodopsin. *J. Gen. Physiol.* 35, 495–517.
- Wang, D., Li, Y., Wang, Z., Sun, G.Y., and Zhang, Q.H. (2013). Nimodipine rescues N-methyl-N-nitrosourea-induced retinal degeneration in rats. *Pharmacogn. Mag.* 9, 149–154.
- Wu, S., Han, G., Milliron, D.J., Aloni, S., Altoe, V., Talapin, D.V., Cohen, B.E., and Schuck, P.J. (2009). Non-blinking and photostable upconverted luminescence from single lanthanide-doped nanocrystals. *Proc. Natl. Acad. Sci. USA* 106, 10917–10921.
- Wu, X., Chen, G., Shen, J., Li, Z., Zhang, Y., and Han, G. (2015). Upconversion nanoparticles: a versatile solution to multiscale biological imaging. *Bioconjug. Chem.* 26, 166–175.
- Wyszecki, G., and Stiles, W.S. (1982). *Color Science: Concepts and Methods, Quantitative Data and Formulae*, Second edition (John Wiley and Sons).
- Xue, T., Do, M.T.H., Riccio, A., Jiang, Z., Hsieh, J., Wang, H.C., Merbs, S.L., Welsbie, D.S., Yoshioka, T., Weissgerber, P., et al. (2011). Melanopsin signaling in mammalian iris and retina. *Nature* 479, 67–73.
- Zhao, L., Ma, W., Fariss, R.N., and Wong, W.T. (2011). Minocycline attenuates photoreceptor degeneration in a mouse model of subretinal hemorrhage microglial: inhibition as a potential therapeutic strategy. *Am. J. Pathol.* 179, 1265–1277.
- Zrenner, E. (2013). Fighting blindness with microelectronics. *Sci. Transl. Med.* 5, 210ps16.

STAR★METHODS

KEY RESOURCES TABLE

| REAGENT or RESOURCE | SOURCE | IDENTIFIER |
|----------------------------------------------------------------------------------------------|--------------------------------------------------|---------------------------------------------------------------------------------------------------------------------------------------------------------------------------------------------------------------|
| Antibodies | | |
| Rabbit polyclonal anti-Iba1 | Wako Pure Chemical Corporation | Cat# 019-19741, RRID: AB_839504 |
| Alexa Fluor 568 goat anti-rabbit IgG (H+L) | Thermo Fisher Scientific | Cat# A-11036, RRID: AB_143011 |
| Chemicals, Peptides, and Recombinant Proteins | | |
| Y ₂ O ₃ | Sigma-Aldrich | Cat# 205168 |
| Yb ₂ O ₃ | Sigma-Aldrich | Cat# 246999 |
| Er ₂ O ₃ | Sigma-Aldrich | Cat# 203238 |
| NOBF ₄ | Sigma-Aldrich | Cat# 175064 |
| Poly(acrylic acid) (PAA) | Sigma-Aldrich | Cat# 323667 |
| 1-ethyl-3-(3-dimethylaminopropyl) carbodiimide hydrochloride (EDC) | TCI America | Cat# D1601 |
| N-hydroxysuccinimide (NHS) | TCI America | Cat# B0249 |
| Concanavalin A (ConA) | Sigma-Aldrich | Cat# C5275 |
| Atropine | Aladdin | Cat# A109524 |
| (R)-(-)-Phenylephrine Hydrochloride | Aladdin | Cat# G1316011 |
| 2,2,2-tribromoethyl alcohol | Sigma-Aldrich | Cat# T48402 |
| 2-Methyl-2-butanol | Sigma-Aldrich | Cat# 240486 |
| Paraformaldehyde | Sigma-Aldrich | Cat# V900894 |
| Optimal Cutting temperature (O.C.T) Compound | Sakura | Cat# 4583 |
| Vitamins | Sigma-Aldrich | Cat# M6895 |
| Non-essential Amino Acid Solution | Sigma-Aldrich | Cat# M7145 |
| Critical Commercial Assays | | |
| TUNEL (Terminal deoxynucleotidyl transferase dUTP nick end labeling) Apoptosis detection kit | Vazyme Biotech | Cat# A113 |
| Experimental Models: Organisms/Strains | | |
| C57BL/6NCrl | Beijing Vital River Laboratory Animal Technology | Cat# 213 |
| <i>Gnat1</i> ^{-/-} | Calvert et al., 2000 | N/A |
| <i>Opn1LW-Cre</i> | Le et al., 2004 | N/A |
| <i>Ai9-lsl-tdTomato</i> | Jackson Laboratory | Cat# 007909 |
| <i>Nrl-GFP</i> | Jackson Laboratory | Cat# 021232 |
| <i>rd1/rd1</i> | Pittler and Baehr, 1991 | N/A |
| <i>cl/cl (cone-DTA)</i> | Soucy et al., 1998 | N/A |
| Software and Algorithms | | |
| Origin 8.0 | OriginLab | https://www.originlab.com/ |
| Igor Pro 8.0 | WaveMetrics | https://www.wavemetrics.com/products/igorpro |
| MATLAB | MathWorks | https://www.mathworks.com/products/matlab.html |
| LAS X | Leica | https://www.leica-microsystems.com/products/microscope-software/details/product/leica-las-x-ls/ |
| LabVIEW | National Instruments, USA | http://www.ni.com/support/labview/ |
| Anilab (China) behavior software | Anilab Software & Instruments, China | http://www.anilab.cn/product.asp |
| ImageJ | National Institutes of Health (NIH), USA | https://imagej.nih.gov/ij/download.html |

(Continued on next page)

Continued

| REAGENT or RESOURCE | SOURCE | IDENTIFIER |
|--------------------------|-----------------------|------------------------|
| Other | | |
| 65 RN 5uL SYR W/O NEEDLE | Hamilton, Switzerland | Cat# 7633-01 |
| RN Needle (34/8 mm/3) | Hamilton, Switzerland | Cat# 207343 |
| 535 nm LED | Starsealand, China | Cat# XL001WP01WBGC/535 |
| 980 nm LED | Starsealand, China | Cat# XL001WP01IRC/980 |
| Photometer | Newport | 1936-R |
| Spectrometer | Avantes | ULS2048 |

CONTACT FOR REAGENT AND RESOURCE SHARING

Further information and requests for resources and reagents should be directed to and will be fulfilled by the Lead Contact, Tian Xue (xuetian@ustc.edu.cn).

EXPERIMENTAL MODEL AND SUBJECT DETAILS

Mice

The experimental procedures on animals followed the guidelines of the Animal Care and Use committee of University of Science and Technology of China. Mice were kept under Specific pathogen Free (SPF) housing facilities, with lighting period of 12h:12h (L:D), constant temperature at 20-24°C and humidity around 40%–70%. The mouse lines in the Key Resources Table and their crossings have been used in this study at the age of 2-3 months. Confirming non-injected mice and PBS-injected mice are identical in retinal histology, we used non-injected mice as control mice in most other experiments. Both male and female mice were used in all experiments.

METHOD DETAILS

Synthesis of pbUCNPs

General chemicals

Y₂O₃ (99.9%), Yb₂O₃ (99.9%), Er₂O₃ (99.9%), CF₃COONa (99.9%), CF₃COOH, 1-octadecene, oleic acid, oleylamine, and other organic solvents were purchased from Sigma-Aldrich and used directly without further purification. Lanthanide trifluoroacetates, Ln(CF₃COO)₃ were prepared according to literature method (Roberts, 1961).

Synthesis of β-NaYF₄:20%Yb, 2%Er core

The β-NaYF₄:20%Yb,2%Er core UCNPs were prepared by a modified two-step thermolysis method (Mai et al., 2006). In the first step, CF₃COONa (0.5 mmol) and Ln (CF₃COO)₃ ((Y+Yb+Er) 0.5 mmol in total, Y:Yb:Er = 78%:20%:2%) precursors were mixed with oleic acid (5 mmol), oleylamine (5 mmol) and 1-octadecene (10 mmol) in a two-neck reaction flask. The slurry mixture was heated to 110°C to form a transparent solution followed by 10 minutes of degassing. Then the flask was heated to 300°C with a rate of 15°C/min under dry argon flow, and it maintained at 300°C for 30 minutes. The β-NaYF₄: Ln intermediate UCNPs were gathered from the cooled reaction solution by centrifugal washing with excessive ethanol (7500 RCF, 30 min). In the second step, the β-NaYF₄: Ln intermediate UCNPs were re-dispersed into oleic acid (10 mmol) and 1-octadecene (10 mmol) together with CF₃COONa (0.5 mmol) in a new two-neck flask. After degassing at 110°C for 10 minutes, this flask was heated to 325°C with a rate of 15°C/min under dry argon flow, and remained at 325°C for 30 minutes. Then, β-NaYF₄: Ln UCNPs were centrifugally separated from the cooled reaction media and preserved in hexane (10 mL) as stock solution.

Synthesis of β-NaYF₄:20%Yb,2%Er@β-NaYF₄ core/shell UCNPs

In this thermolysis reaction, as-synthesized-NaYF₄:20%Yb, 2%Er UCNPs served as cores for the epitaxial growth of undoped-NaYF₄ shells. Typically, a stock solution of β-NaYF₄: 20%Yb, 2%Er UCNPs (5 mL, ca. 1 μmol/L core UCNPs) was transferred into a two-neck flask and hexane was sequentially removed by heating. CF₃COONa (0.5 mmol) and Y(CF₃COO)₃ (0.5 mmol) were added along with oleic acid (10 mmol) and 1-octadecene (10 mmol). After 10 minutes of degassing at 110°C, the flask was heated to 325°C at a rate of 15°C/min under dry argon flow and was kept at 325°C for 30 minutes. The products were precipitated by adding 20 mL ethanol to the cooled reaction flask. After centrifugal washing with hexane/ethanol (7500 RCF, 30 min), the core/shell UCNPs were collected and re-dispersed in 10 mL of hexane.

Synthesis of pbUCNPs

As synthesized β-NaYF₄:20%Yb,2%Er@β-NaYF₄ UCNPs were first treated by surface ligand exchange using a modified literature method (Dong et al., 2011). Generally, nitrosonium tetrafluoroborate/DMF solution (0.2 g NOBF₄, 5 mL DMF) was added into 1 mL UCNPs hexane stock solution, followed by 4 mL hexane and 3 hours of stirring at room temperature. Then oleic acid-free UCNPs

were precipitated by adding 5 mL isopropanol and purified by centrifugal wash with DMF. UCNP solids were re-dispersed in poly (acrylic acid)/DMF (10 mg/mL, 5 mL) solution to coat UCNP surface with PAA. After overnight stirring, PAA coated UCNPs (paaUCNPs) were purified by centrifugal and wash with DI-water. Then ConA proteins were conjugated to paaUCNPs surface by traditional EDC/NHS coupling. Generally, 10 mg paaUCNPs in 1 mL DI-water were treated with 1 μ L EDC/NHS water solution (1 g/L). After stirring at room temperature for 1 hour, 30 μ L ConA solution was introduced (5 g/L) and the mixture was further stirred overnight. The pbUCNPs were purified by washing with deionized water, centrifugation and dispersed in water for further use.

Sub-retinal injection

For sub-retinal injection, pupils were dilated with atropine (100 μ g/mL, Sigma-Aldrich), and animals were anesthetized by Avertin (450 mg/kg, Sigma-Aldrich). A 33 Gauge needle was inserted through the cornea to release the intra-ocular pressure. Nanoparticles dissolved in 2 μ L sterile PBS to reach 25 mg/ml was injected into the sub-retinal space through a beveled, 34-gauge hypodermic needle (Hamilton, Switzerland). During and after the injection the animal was kept on a warming blanket and eyes were kept wet to avoid cataract.

Distribution and spectrum analysis

To observe the distribution of nanoparticles in the sub-retinal space, fresh retinas were isolated from eyes following execution. Retinas were then fixed in 4% paraformaldehyde (PFA), frozen and cut into 20 μ m slices with Leica CM3050 S Cryostat (Leica, Germany) (Figure 1). All retinal slices were scanned by Leica two-photon microscope (SP8, Leica, Germany). The excitation spectrum was obtained by exciting the nanoparticles with two-photon laser beam (wavelength from 700-1040 nm, $\Delta\lambda = 5$ nm), and emitted light intensity was measured at 535 nm. The emission spectrum was obtained by exciting nanoparticles with a 980 nm laser beam and collecting the emitted light with a photomultiplier behind a light grating slit with 5 nm wavelength step from 435 nm to 790 nm (SP8, Leica, Germany). Data were acquired with Leica Imaging software and analyzed with Origin 8.0 (Origin Lab Corp). High resolution fluorescence images of rods and cones were confocal images with 63 \times oil immersion objective from 6- μ m retina slices.

Retinal histology

To analyze whether nanoparticles are potentially toxic to retina, we injected nanoparticles in different concentrations and then performed hematoxylin-eosin (HE) staining on fixed retinal slices (Burstyn-Cohen et al., 2012). Cell bodies of photoreceptors were located in the outer nucleus layer (ONL) and we counted the number of cell layers as a parameter to evaluate the damage. The number of cell layers were counted at 5 different locations of injection sites and repeated at 5 randomly selected different slices of each retina, then averaged.

TUNEL Apoptosis detection

We detect photoreceptors apoptosis using TUNEL (Terminal deoxynucleotidyl transferase dUTP nick end labeling) Apoptosis detection kit (Vazyme Biotech, Ltd-A113). Before TUNEL staining, retinal slices were washed twice by PBS solution and then incubated in 1% Triton X-100 (Sangon-A110694) solution for 2-3 hours. Afterward retinal slices were equilibrated in equilibration buffer (provided in the kit) for 10-30 min and then incubated in TdT incubation buffer for 60 min. Finally, retinal slices were incubated in DAPI-PBS solution for 5 min and then washed 3 times by PBS solution. All retinal slices were scanned by Leica two-photon microscope to detect TUNEL signals. The number of positive cells were counted at 6 different locations of injection site from each retina and then averaged.

Microglia staining

To detect immune reactions in nanoparticles injected retinas, we implemented Iba1 (ionized calcium binding adaptor molecule 1, one marker protein of microglia) staining assay. Retinal slices were washed twice by PBS solution and then blocked in 1% Triton X-100 (Sangon-A110694) and 5% goat serum solution (blocking solution) for 2-3 hours. Then slices were incubated in blocking solution with rabbit anti-Iba1 antibody (Wako-019-19741, 1:1000) at 4°C overnight. Afterward, slices were washed 3 times by PBS solution, and then incubated in Alexa Fluor 568 goat anti-rabbit IgG (H+L) secondary antibody (Thermo Fisher Scientific-1832035, 1:800) at room temperature for 2-3 hours. Finally, retinal slices were incubated in DAPI-PBS solution for 5 min and then washed 3 times by PBS solution. All retinal slices were scanned by Leica two-photon microscope to analyze retinas immune activities. The number of positive cells were counted at 6 different locations of injection site from each retina and then averaged.

Single cell electrophysiology

Before rod suction pipette recordings, pbUCNP-injected or non-injected mice were dark-adapted overnight. Animals were anesthetized with Tribromoethanol (Avertin, 450 mg/kg, Sigma-Aldrich) and eyes were enucleated after euthanasia. Retina was carefully isolated from the eye and flat-mounted onto the recording chamber. Recordings were carried out on an Olympus upright infrared-DIC microscope. The extracellular bath solution was bicarbonate-buffered Ames medium (in mM): 120 NaCl, 22.6 NaHCO₃, 3.1 KCl, 0.5 KH₂PO₄, 1.5 CaCl₂, 1.2 MgSO₄, 6 Glucose, equilibrated with 5% CO₂/95% O₂ and heated to 35°C (Warner Instruments Corp, TC-3448). The perfusion speed was \sim 5 ml/min through the 3 mL recording chamber. The outer segment of a rod was gently sucked into a \sim 1.6 μ m diameter glass pipette filled with modified Ames solution (in mM): 135 NaCl, 10 mM HEPES, 3.1 KCl, 0.5 KH₂PO₄, 1.5 CaCl₂, 1.2 MgSO₄, 6 Glucose, pH adjusted to 7.4 by NaOH. Stimulation light was applied through the imaging objective.

535-nm light was from a filter block in front of a white light LED. Infrared light was generated by 980-nm laser. Flash light intensities in Figures 3B–3E, S4A, S4B, S4D, S4E, S4G, and S4H: 535-nm - 0.64, 2.57, 12.55, 49.38, 162.5, 1102.21; 980-nm - 1.50×10^5 , 6.31×10^5 , 1.85×10^6 , 5.81×10^6 , 2.26×10^7 , 1.17×10^8 ; unit - photons $\cdot \mu\text{m}^{-2}$.

To measure the action spectrum of rods, light flashes in a series of wavelengths were delivered to elicit flash photoresponses. All the recorded rods were given a strong light test pulse to check if a normal saturating photocurrent can be elicited, before the family of light pulses with different wavelengths was given. Flash light intensities were selected to generate photocurrents within the linear range. Light pulses were from LEDs or lasers. The sensitivity was calculated as photoresponse / (flash intensity \times area) and then normalized to the peak sensitivity.

To quantify light adaptation, we applied background light and allowed at least 2-min adaptation for the recorded rod (Karnas et al., 2013; Schmidt and Kofuji, 2010). Then on top of the background light, a light flash was applied to elicit a transient photocurrent. Flash sensitivity (S_F) was calculated by dividing the peak amplitude of the transient photocurrent with the intensity of the flash light. For a series of applied background light with different intensities, flash sensitivities were measured and normalized to the flash sensitivity in the dark (S_D). The background light intensities are: 535-nm - dark, 12.9, 49.20, 113.24, 266, 542.79, 2700.06, 5965.32; 980-nm - dark, 4.08×10^6 , 1.03×10^7 , 2.02×10^7 , 4.60×10^7 , 7.44×10^7 , 1.94×10^8 , 4.36×10^8 ; unit - photons $\cdot \mu\text{m}^{-2} \cdot \text{s}^{-1}$). The intensity-response curves except under dark background were measured under three different conditions: visible light flashes on top of a visible or NIR light background (535-nm - 776 photons $\cdot \mu\text{m}^{-2} \cdot \text{s}^{-1}$ or 980-nm - 1.3×10^8 photons $\cdot \mu\text{m}^{-2} \cdot \text{s}^{-1}$) and NIR light flashes on top of a visible light background (535-nm - 776 photons $\cdot \mu\text{m}^{-2} \cdot \text{s}^{-1}$).

Data were lowpass filtered at 50 Hz and sampled at 25 kHz by Axon 700B Amplifier and Digital 1440A interface. Data were analyzed with custom routines in Origin 8.0 and presented as mean \pm SD. Single cell electrophysiology was carried out 5–6 weeks after pbUCNPs injection. Data for noise analysis of rods were filtered with low-pass Bessel filter (cutoff frequency - 5Hz) (Baylor et al., 1980; Fu et al., 2008). Power spectra density was calculated with function 'periodogram()' in MATLAB (Mathworks, USA).

Electroretinography

Mice were anesthetized by Avertin (450 mg/kg, Sigma-Aldrich) after their pupils were dilated with atropine (100 $\mu\text{g}/\text{mL}$, Sigma-Aldrich). During the experiment, the anesthetized animal was kept on a warming blanket and eyes were kept wet to avoid cataract (Dalke et al., 2004). Mice were placed into a Faraday cage and a glass recording electrode with a tip diameter of 10 μm was put tightly against the center of the cornea. A ground electrode was inserted into subcutaneous space of the tail and a reference electrode was inserted into subcutaneous space of the head. A 535-nm LED light (8.26×10^3 photons $\cdot \mu\text{m}^{-2}$) and a 980-nm laser beam with a spot diameter of 1.8 mm (9.83×10^8 photons $\cdot \mu\text{m}^{-2}$) was placed in front of the pupil for stimulation. Data acquisition was carried out by a differential amplifier (AM-SYSTEM INC) and Digital 1440A (Axon CNS). Data were analyzed with custom routines in Origin 8.0 (Origin Lab Corp). ERG was carried out 4 weeks after pbUCNPs injection.

Pupillary light reflex

Head-fixed mice were used for pupillometry of long-duration measurements (Xue et al., 2011). C57BL/6 wild-type mice were anesthetized with intraperitoneal injection of Avertin. A patch of skin overlying the skull was excised, and four bone screws were threaded into the skull, with care taken to prevent any damage to the brain. These screws were covered with dental cement, and served as the foundation for a stainless-steel post. Under anesthesia, eyes were kept wet with eye gel (5% Sodium carboxymethyl cellulose in PBS, Sigma-Aldrich) to avoid cataract. Mice were kept in 12/12 hours light/dark cycles. All PLR experiments were performed during the day: from 2 hours after light-on to 2 hours before light-off with > 1 h dark adaptation. To measure the PLR of the pbUCNP-injected eye, we built a pupillometer with a miniature, infrared CCD camera and 850-nm LED light for video recording via a Ganzfeld sphere. A laser beam with a spot diameter of 1.8 mm was placed 1 mm away in front of the injected eye. Light intensity of 980-nm light in Figure 4B: paaUCNP-injected - 9.49×10^7 , 2.36×10^8 , 3.80×10^8 , 6.67×10^8 , 1.42×10^9 , 2.97×10^9 , 4.44×10^9 , 6.06×10^9 , 1.13×10^{10} , 1.97×10^{10} , 2.56×10^{10} ; pbUCNP-injected - 1.33×10^6 , 3.15×10^6 , 1.01×10^7 , 2.44×10^7 , 4.18×10^7 , 6.54×10^7 , 1.21×10^8 , 1.72×10^8 , 2.80×10^8 ; unit - photons $\cdot \mu\text{m}^{-2} \cdot \text{s}^{-1}$. Videos for contralateral eyes were recorded at a frame rate of 5 Hz. A data-acquisition board (NI USB-6211, National Instruments) and custom written software were used for triggering recordings and light stimulations. Videos were recorded and analyzed with XCAP-Ltd V3.x. The normalized pupil area was calculated by normalizing the area measured at maximum constriction during the 40 s light stimulation to that before light stimulation. We measured PLR of injected mice 2–3 weeks after injection.

Light-dark box

Mice were placed in a 59 cm \times 28.5 cm \times 28.5 cm custom-made light and dark double box (Bourin and Hascoët, 2003). On the three sides of the light box, 20 980-nm LEDs (1 Watt) and twenty 535-nm LEDs (1 Watt) were evenly placed for light stimulation. Intensity of 980 nm light at the center of the light box was 8.1×10^7 photons $\cdot \mu\text{m}^{-2} \cdot \text{s}^{-1}$, and intensity of 535-nm light was 9.1×10^2 photons $\cdot \mu\text{m}^{-2} \cdot \text{s}^{-1}$. Animals were introduced to the box and allowed for 5-min adaptation. A series of light stimulation in the order of 5 min in dark, 5 min in 980-nm light, and 5 mins in 535-nm light was programmed. All these experiments were carried out in the dark environment and videos were acquired by an infrared camera and custom-made software. Experiments were performed 4–5 weeks after injection.

Light induced fear conditioning

Fear conditioning experiments were carried out in a 21.5 cm × 21.5 cm × 24 cm custom-made box (Cui et al., 2013) (Figure 4E). On the four sides of the box, 20 980-nm LEDs (1 Watt) and 20 535-nm LEDs (1 Watt) were evenly placed for light stimulation. The training protocol consisted of 5-min adaptation, 20 s 535-nm light as conditional stimulus (CS) followed with a 2 s electrical foot shock as unconditional stimulus (US). Paired CS and US was repeated 5 times with 2-min interval. One day after the training, a test protocol, which was the same as the training protocol but no unconditional stimulus (US), was used to test freezing time of mice and in which 2 times 20 s 535-nm light and 2 times 980-nm light randomly as conditional stimulus (CS). Anilab (China) behavior software was used to control 980-nm or 535-nm LEDs light stimulation and the electrical shock. Intensity of 980-nm light at the center of the box was 1.07×10^8 photons $\cdot \mu\text{m}^{-2} \cdot \text{s}^{-1}$, and intensity of 535-nm light was 1.47×10^3 photons $\cdot \mu\text{m}^{-2} \cdot \text{s}^{-1}$. Freezing time ratios of Pre-CS (40 s before conditional stimulus) and CS (40 s, total time of the 2 times 980-nm or 535-nm conditional stimulus) were analyzed to compare the effect of light induced freezing. Experiments were conducted 4-5 weeks after injection.

Visually evoked potential

1-2 weeks after pbUCNPs injection, VEP was carried out as described in literatures (Cooke and Bear, 2013; Cooke et al., 2015). Mice were anesthetized by pentobarbital sodium (LUPI-P8410) at the dose of 1 g/kg body weight and then fixed on the stereotaxic apparatus. The skull on either right or left visual cortex was grinded off and removed carefully avoiding any damage to the visual cortex. An electrical recording glass pipette with a tip diameter of 15 μm was inserted into right/left visual cortex and targeted to the following coordinates (relative to bregma): 1-(2.15, -2.8, -0.4), 2-(2.75, -2.8, -0.4), 3-(2.0, -3.28, -0.4), 4-(2.75, -3.28, -0.4), 5-(2.25, -4.24, -0.4), 6-(3.0, -4.24, -0.4) mm. A ground electrode was inserted into subcutaneous space of the tail and a reference electrode was inserted into subcutaneous space of the head. The contralateral eye of the exposed visual cortex was illuminated by 980-nm light (7.07×10^8 photons $\cdot \mu\text{m}^{-2} \cdot \text{s}^{-1}$) or 535-nm light (3.37×10^3 photons $\cdot \mu\text{m}^{-2} \cdot \text{s}^{-1}$) during recording. Signal was amplified by a differential amplifier (AM-SYSTEM INC) and digitized by Digital 1440A (Axon CNS).

Y shaped water maze

Y-shaped water maze experiments were performed in either scotopic (dark) or photopic (light) condition (Prusky et al., 2000). During adaptation periods, mice were released in the water close to stimulating light boxes for discovering the hidden platform. During adaptation period, the released place became further from the light boxes with time and ultimately mice were released at the release chute. The adaptation lasted for 2 days with one section (12 trials per section) per day. After adaptation mice were trained to find a hidden platform associated to the task stimuli. Trainings usually lasted for 7 days: one section per day and 12 trials per section. The platform and the associated stimuli were placed right or left randomly across trials in each section, such as LRLRLRLRLRL. Upon completion of the trainings, the test sections were conducted in two separated days. In Task #1 animals were trained with visible light horizontal and vertical light gratings (0.8 circles per degree, c/d, 7.26×10^3 photons $\cdot \mu\text{m}^{-2} \cdot \text{s}^{-1}$ at the release chute) and then tested to discriminate visible (7.26×10^3 photons $\cdot \mu\text{m}^{-2} \cdot \text{s}^{-1}$ at the release chute) and NIR (8.01×10^7 photons $\cdot \mu\text{m}^{-2} \cdot \text{s}^{-1}$ at the release chute) horizontal/vertical light gratings in the dark background. For the visual acuity test in the dark background, 0.054 c/d, 0.08 c/d, 0.107 c/d, 0.134 c/d, 0.161 c/d, 0.214 c/d, 0.268 c/d, 0.322 c/d, 0.35 c/d, 0.38 c/d, 0.435 c/d gratings were tested for 980-nm light stimuli (8.01×10^7 photons $\cdot \mu\text{m}^{-2} \cdot \text{s}^{-1}$ at the release chute) and 535-nm light stimuli (7.26×10^3 photons $\cdot \mu\text{m}^{-2} \cdot \text{s}^{-1}$ at the release chute). In Task #2 animals were trained and tested to discriminate NIR light gratings made of LEDs arrays under the background visible room light (background light intensity equivalent to 535-nm light was 4.31×10^3 photons $\cdot \mu\text{m}^{-2} \cdot \text{s}^{-1}$). Two lines of 535-nm LEDs and two lines of 980-nm LEDs were placed perpendicular to each other. Each line was made of 18 LEDs. The left pattern was 90 degrees rotated compared to the right pattern. The training lasted for 9 days with one section per day and 12 trials per section with 980-nm LEDs on only. In Task #2, the intensity of 980-nm light pattern measured at the release chute was 8.01×10^7 photons $\cdot \mu\text{m}^{-2} \cdot \text{s}^{-1}$ and 535-nm light pattern was 7.26×10^3 photons $\cdot \mu\text{m}^{-2} \cdot \text{s}^{-1}$. In Task #3 animals were trained with visible light triangle and circle patterns and tested to discriminate visible and NIR light triangle/circle patterns under the dark background. In Task #4 animals were tested to discriminate visible light triangle/circle patterns under the visible light background (7.26×10^3 photons $\cdot \mu\text{m}^{-2} \cdot \text{s}^{-1}$) or NIR light background (8.01×10^7 photons $\cdot \mu\text{m}^{-2} \cdot \text{s}^{-1}$). In Task #3 and #4, the intensity of 980-nm light pattern measured at the release chute was 8.01×10^7 photons $\cdot \mu\text{m}^{-2} \cdot \text{s}^{-1}$ and 535-nm light pattern was 7.26×10^3 photons $\cdot \mu\text{m}^{-2} \cdot \text{s}^{-1}$. In Task #5 animals were tested to discriminate patterns in the mixture of visible and NIR light patterns. The hidden platform was associated with the triangle pattern and four different stimuli were presented randomly (see Figure 6I). In Task #5, the intensity of 980-nm light pattern measured at the release chute was 2.32×10^8 photons $\cdot \mu\text{m}^{-2} \cdot \text{s}^{-1}$ and 535-nm light pattern was 1.57×10^3 photons $\cdot \mu\text{m}^{-2} \cdot \text{s}^{-1}$. All videos were acquired by infrared camera and analyzed by Corel Screen Cap X6 and Origin 8.0. Y shaped water maze experiments were implemented 3-8 weeks after pbUCNP-injection. The spectrum of 980-nm LEDs was measured using spectrometer (Avantes USB2.0) to confirm there is no detectable visible light emission.

QUANTIFICATION AND STATISTICAL ANALYSIS

Imaging quantifications

Fluorescence analysis was based on careful match of the confocal imaging parameters. The intensities of pixels or the number of cells were then quantified in ImageJ (NIH).

Statistics

Statistical analysis was performed using Microsoft Excel or Matlab softwares. Unpaired two-tailed Student's test was used to determine statistical significance. The “n” numbers for each experiment are provided in the text and figure legends. Data are all presented as mean \pm SD. For immunocytochemistry and toxicological detection experiments were repeated on at least 3 animals.

Fitting procedures

Fittings were conducted in MATLAB (Mathworks, USA) with an unconstrained nonlinear optimization routine. The upconversion relationship was fitted by a linear function in the log-log scale. The dose response curve of PLR - the normalized pupil area versus light intensity - was fitted by the Hill function. The action spectrum of rods was fitted to absorption-spectrum template (Fu et al., 2008; Govardovskii et al., 2000). The relative flash sensitivity of background light adapted rods was fitted to Weber-Fechner equation (Baylor et al., 1980; Morshedian et al., 2018; Fu et al., 2008).

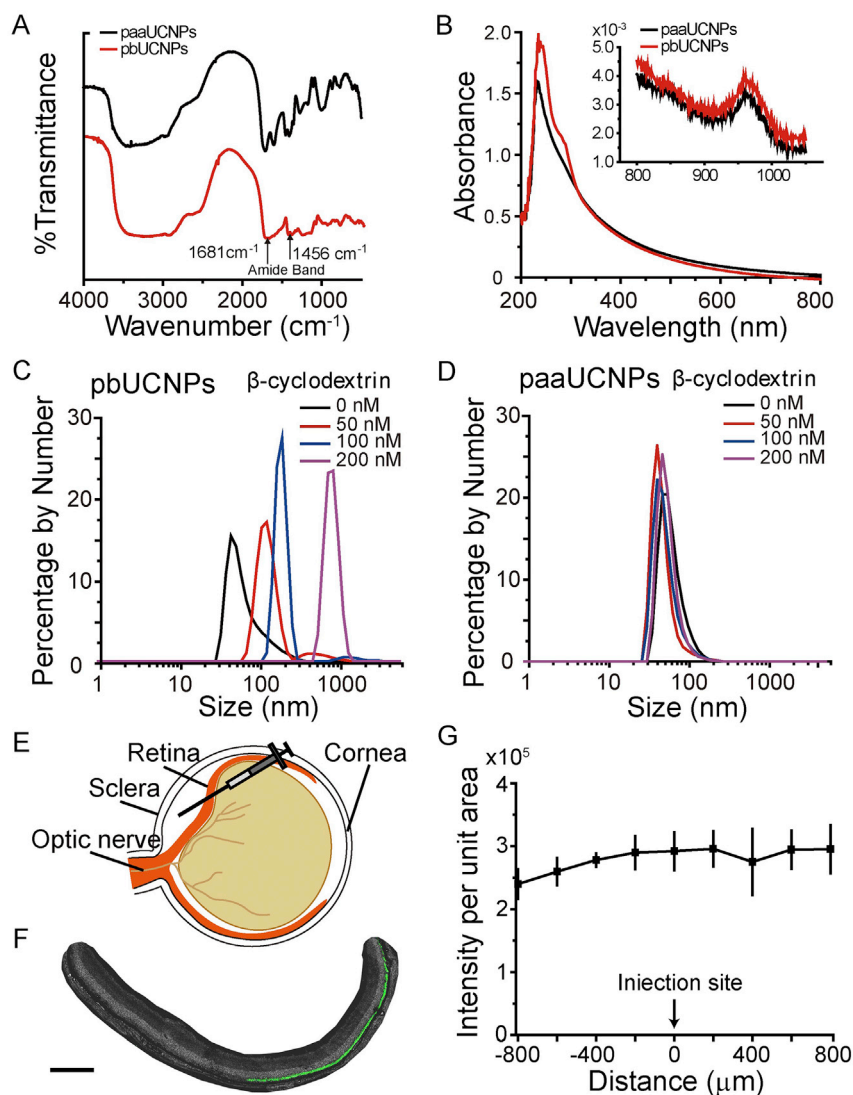


Figure S1. Properties of UCNPs and Distributions in Subretinal Space, Related to Figure 1

(A) Fourier Transform-Infrared (FT-IR) spectra of UCNPs before (black) and after (red) ConA surface modifications. After ConA conjugation, new peaks at 1681 and 1456 cm^{-1} emerged, which are attributed to amide bond formation.

(B) Absorption spectrum of UCNPs before (black) and after (red) ConA conjugation.

A new absorption peak at 285 nm is assigned to ConA. NIR range absorption is shown in inset, and the absorption peak at 980 nm is attributed to the absorption for upconversion.

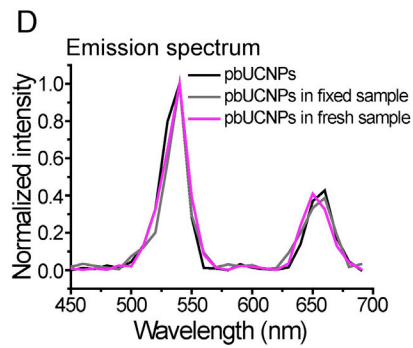
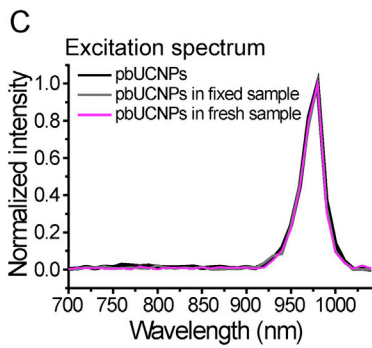
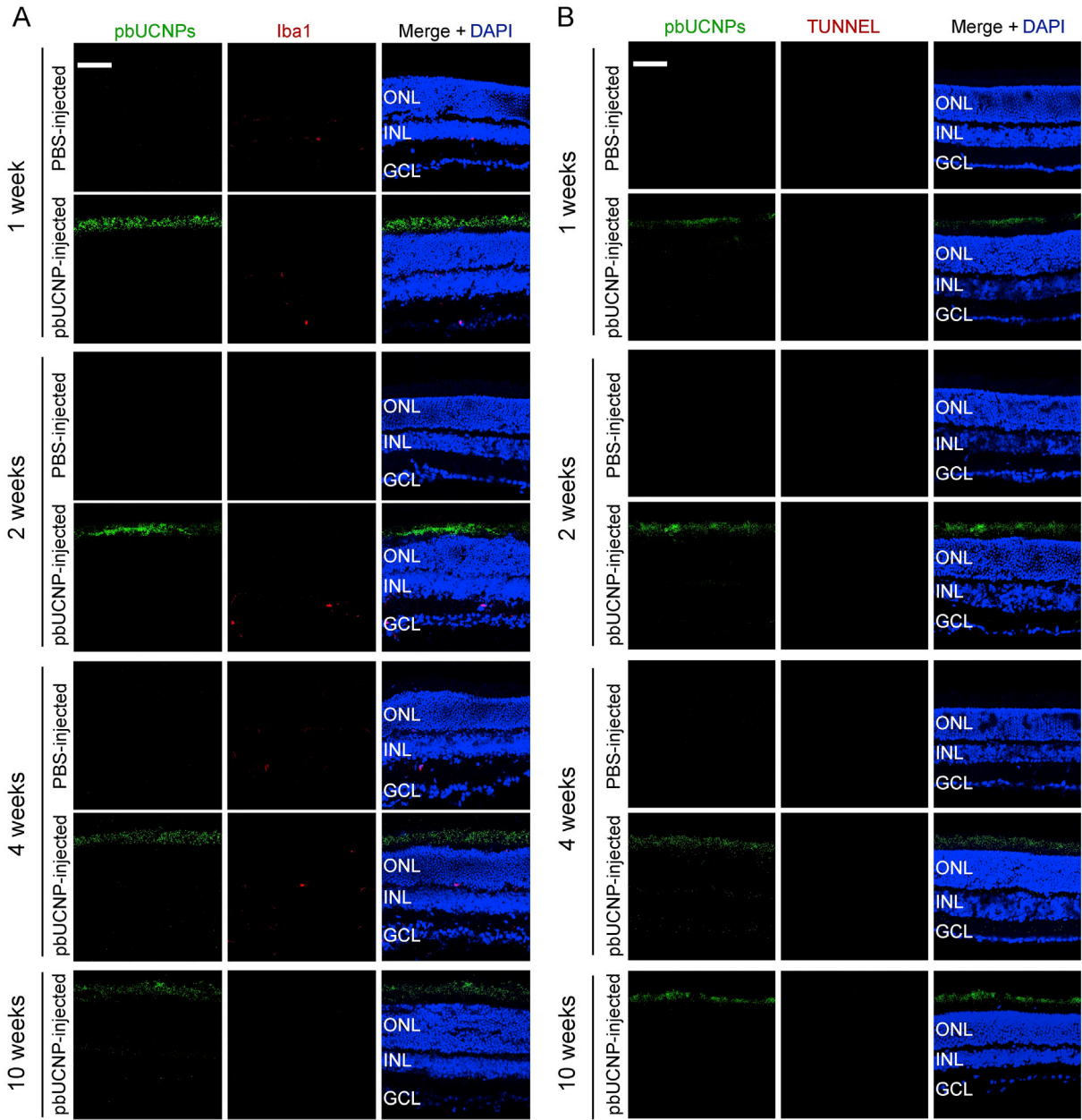
(C) Dynamic light scattering (DLS) spectrum of pbUCNPs (0.2 mg/mL) upon the introduction of different concentrations of β -cyclodextrins (0, 50, 100 and 200 nM) showing aggregation of pbUCNPs.

(D) Dynamic light scattering spectrum of paaUCNPs (0.2 mg/mL) upon the introduction of different concentrations of β -cyclodextrins (0, 50, 100 and 200 nM).

(E) Illustration of subretinal injection of pbUCNPs.

(F) Distribution of pbUCNPs (green) in the subretinal space after a single injection. Scale bar: 250 μm .

(G) Quantified green light intensity distribution along the spread of pbUCNPs in the subretinal space ($n = 4$). Data are mean \pm SD. X axis is the distance from the injection site and y axis is the total green pbUCNPs emission intensity from a $50 \times 50 \mu\text{m}^2$ measuring window on a retina slice along the distribution of pbUCNPs from the injection site.



(legend on next page)

Figure S2. Toxicity and Biocompatibility Evaluation of Retina Slices in a Time Series up to 10 Weeks after Injection, Related to Figure 2

(A) Microglia marker Iba1 staining of retina slices. Retinal injection of 6 mM H₂O₂ was used as the positive control. Red: Iba1; Green: pbUCNPs emission upon excitation by NIR light; Blue: DAPI (4', 6-diamidino-2-phenylindole) signal indicating cell nucleuses. Scale bar: 50 μm.

(B) TUNEL staining of retina slices. Retinal injection of 6 mM H₂O₂ was used as the positive control. Red: TUNEL staining; Green: pbUCNPs emission upon excitation by NIR light; Blue: DAPI. Scale bar: 50 μm.

(C) and (D) Excitation (C) and emission (D) spectra of pbUCNPs in solution (black), fixed retina (gray) and fresh retina (violet).

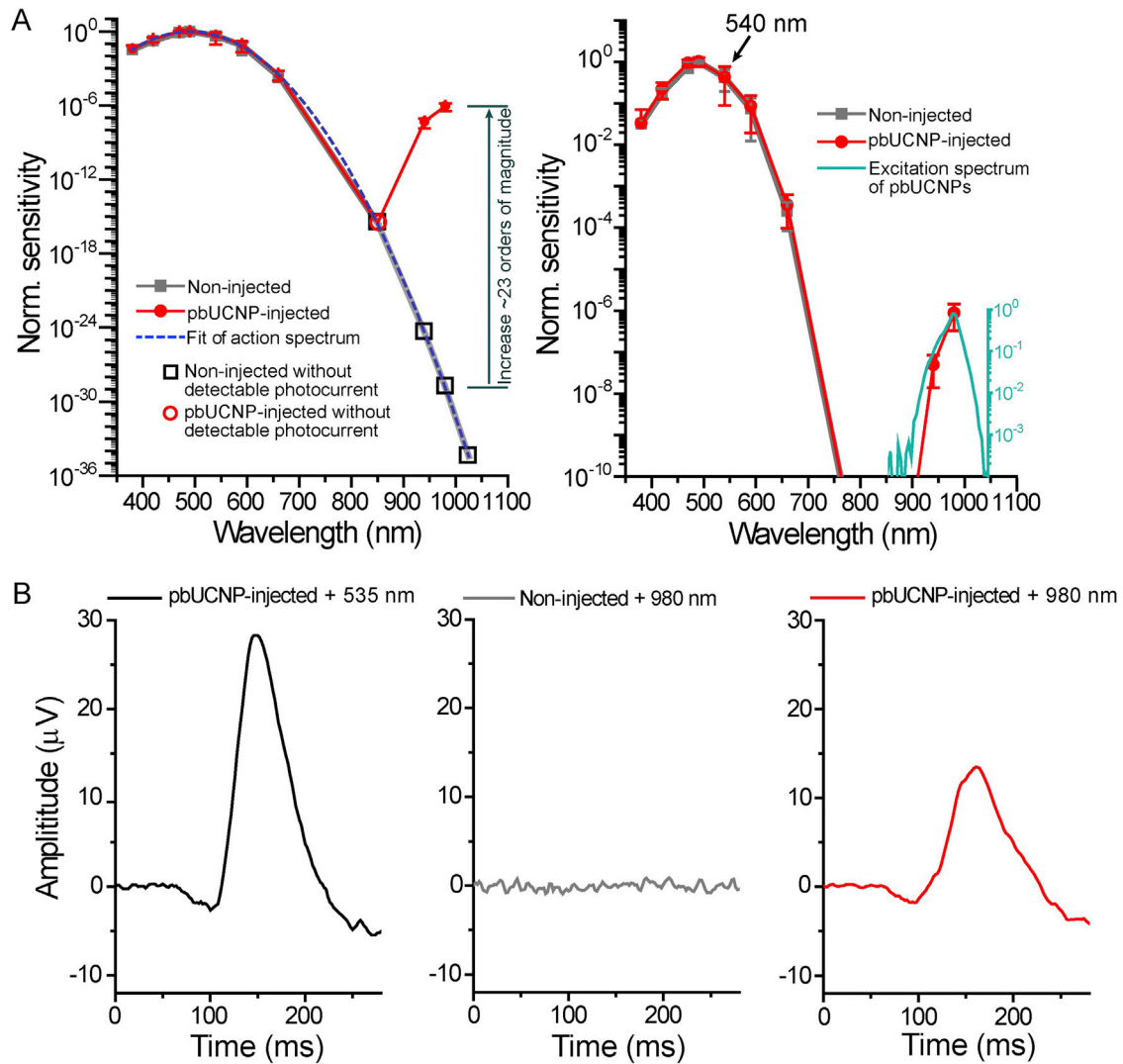


Figure S3. Action Spectra of Rods and ERG of *Gnat1*^{-/-} Mice, Related to Figure 3

(A) *Left:* Action spectra of rods from non-injected (gray) and pbUCNP-injected (red) retina. Fit of action spectrum of rods from non-injected retina to absorption-spectrum template (Fu et al., 2008; Govardovskii et al., 2000) is shown in dashed blue line. Open squares are theoretical predicted values from the fit under detection threshold. The predicted sensitivity of non-injected rods to the NIR light (980 nm) is extremely small. With the help of pbUCNPs, rods gained 23 orders of magnitude higher sensitivity to 980-nm NIR light. *Right:* Same action spectra were plotted with excitation spectrum of pbUCNPs (cyan) normalized to the action spectrum value at 980 nm of rods from pbUCNP-injected mice. All data are mean \pm SD.

(B) ERG recordings of *Gnat1*^{-/-} mice. Light intensities are 7.26×10^3 photons $\cdot \mu m^{-2}$ for 535-nm light and 8.01×10^7 photons $\cdot \mu m^{-2}$ for 980-nm light.

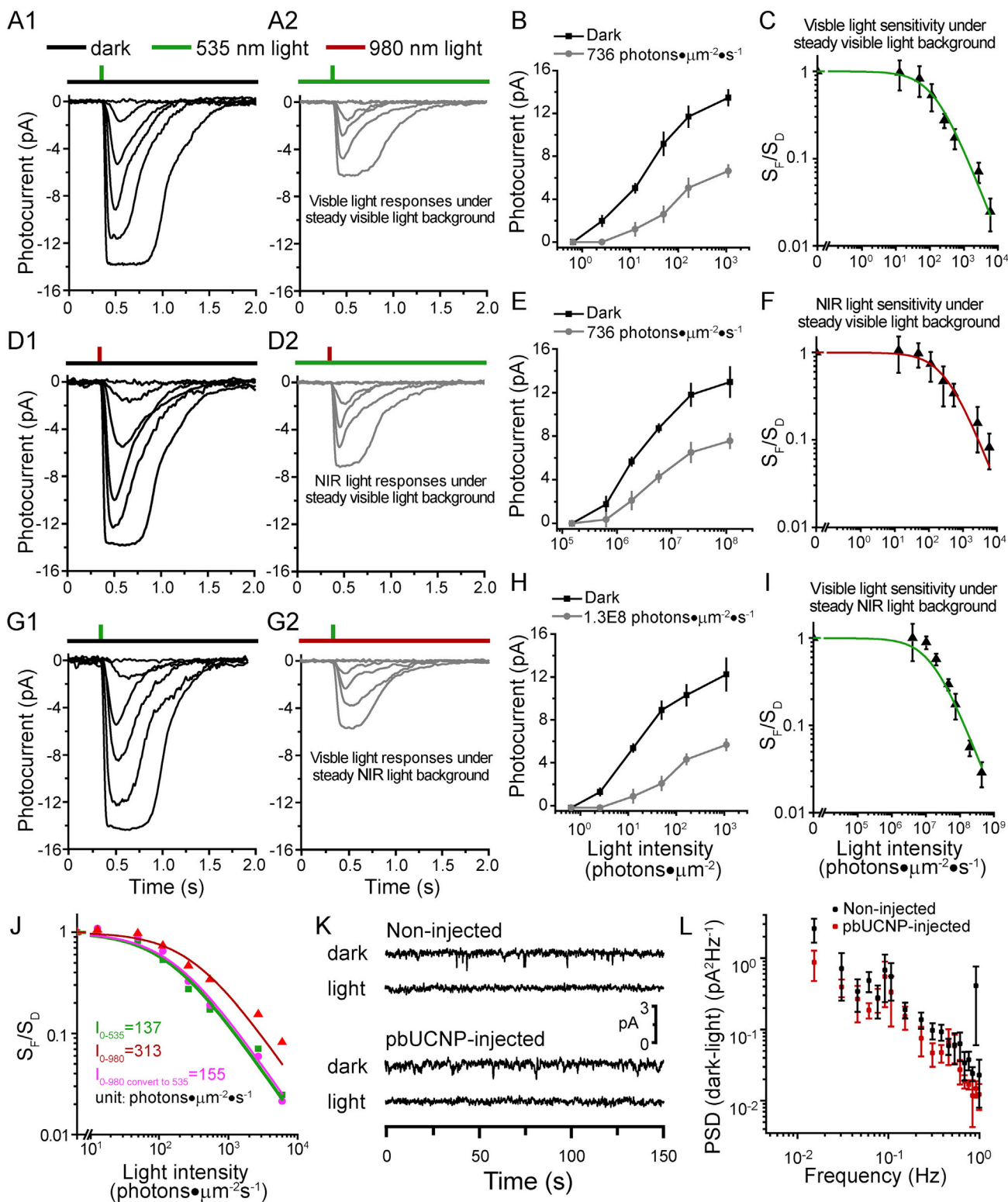


Figure S4. Adaptation and Noise Properties of Rods from pbUCNP-Injected Retina, Related to Figure 3

(A) Visible light flash responses of rod photoreceptors under dark and visible light background. Background and flash light stimulations are illustrated on top of the recording traces (A, D and G).

(legend continued on next page)

- (B) Intensity-response curves of rods in (A) under dark background (black trace) and the specified background with 535-nm light intensity of $736 \text{ photons} \cdot \mu\text{m}^{-2} \cdot \text{s}^{-1}$ (gray trace) ($n = 3$). All data are mean \pm SD.
- (C) Normalized flash sensitivity is plotted as a function of background light intensity and fitted with Weber-Fechner equation $S_F/S_D = 1/[1+I_B/I_0]$ (Baylor et al., 1980; Morshedien et al., 2018; Fu et al., 2008). The visible background light intensity that decreased the visible flash light sensitivity by half, $I_{0(V/V)}$, is $137 \text{ photons} \cdot \mu\text{m}^{-2} \cdot \text{s}^{-1}$, similar to values in previous studies (Karnas et al., 2013; Schmidt and Kofuji, 2010) ($n = 3$). All data are mean \pm SD.
- (D) NIR light flash responses of rod photoreceptors under dark and visible light background.
- (E) Intensity-response curve of rods in (D) under dark background and the specified background 535-nm light intensity of $736 \text{ photons} \cdot \mu\text{m}^{-2} \cdot \text{s}^{-1}$ ($n = 3$).
- (F) Normalized flash sensitivity is plotted as a function of background light intensity and fitted with Weber-Fechner equation ($n = 3$). The visible background light intensity that decreased the NIR flash light sensitivity by half, $I_{0(N/V)}$, is $313 \text{ photons} \cdot \mu\text{m}^{-2} \cdot \text{s}^{-1}$.
- (G) Visible light flash responses of rod photoreceptors under dark and NIR light background.
- (H) Intensity-response curve of rods in (G) under dark background and the specific background light intensity of $1.3 \times 10^8 \text{ photons} \cdot \mu\text{m}^{-2} \cdot \text{s}^{-1}$ ($n = 3$).
- (I) Normalized flash sensitivity is plotted as a function of background light intensity and fitted with Weber-Fechner equation ($n = 3$). The NIR background light intensity that decreased the visible light flash sensitivity by half, $I_{0(N/N)}$, is $2.76 \times 10^7 \text{ photons} \cdot \mu\text{m}^{-2} \cdot \text{s}^{-1}$. All data are mean \pm SD.
- (J) Adaptation of visible (green) and NIR (red) light flash sensitivity under the visible light background (from C and F) were re-plotted. The discrepancy came from the nonlinearity of upconversion by pbUCNPs (as quantified in Figure S5B). NIR light flash adaptation (red) was converted to equivalent visible light flash adaptation (violet) according to the pbUCNP upconversion relation fit from Figure S5B, which matched very well with the visible light flash adaptation curve (green).
- (K) Representative traces of dark current and steady-light current from rods of non-injected and pbUCNP-injected mice.
- (L) Differential power spectrum density between dark and light current was the difference between the power spectrum density in darkness and in saturated steady light (Baylor et al., 1980; Fu et al., 2008). There is no significant difference in the rod dark current noise spectrum with respect to non-injected versus pbUCNP-injected animals, indicating that pbUCNPs did not interfere with the membrane biophysical properties and the phototransduction cascade of rods. All data are mean \pm SD.

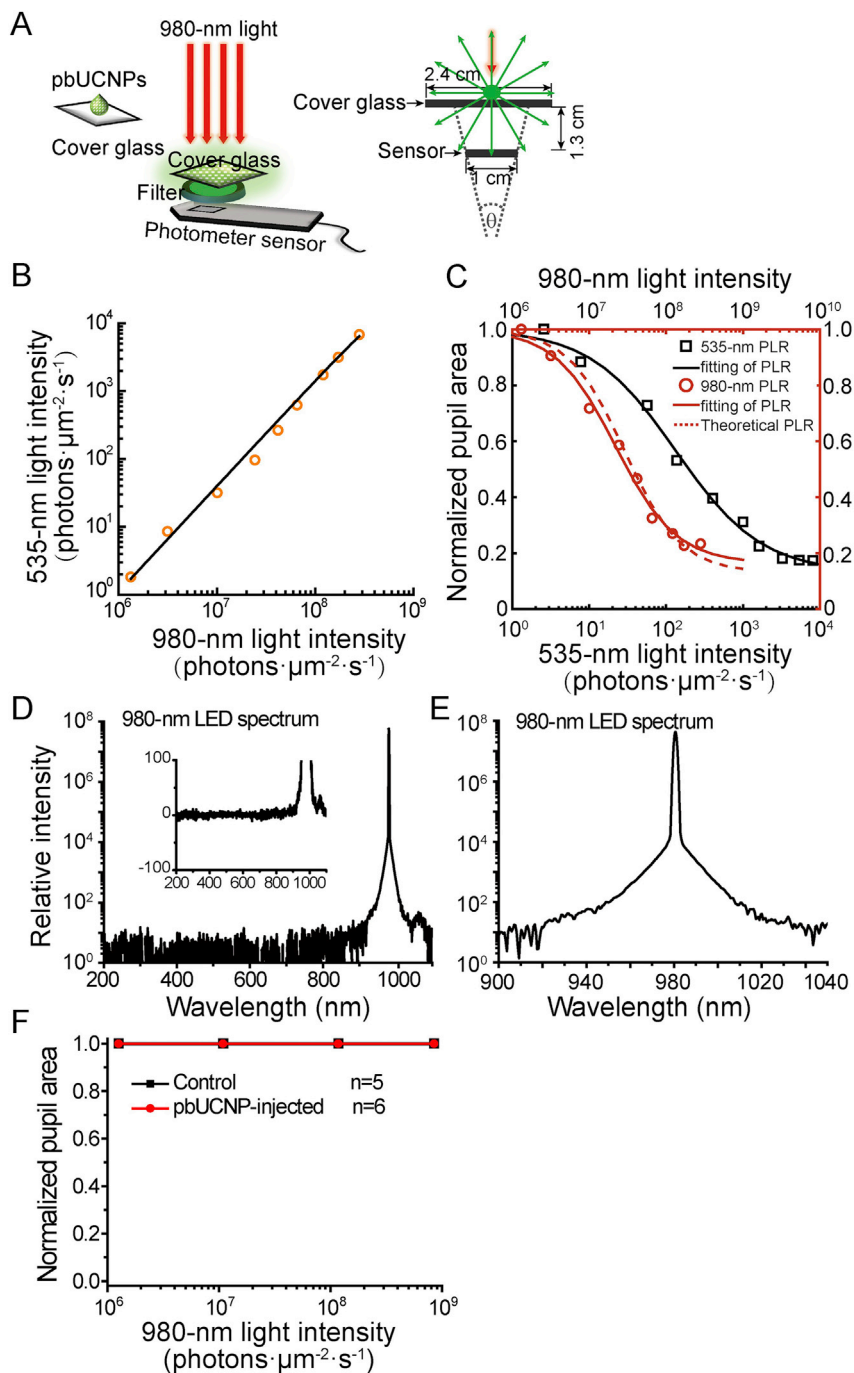


Figure S5. Demonstration of the Nonlinearity of pbUCNP Photon Upconversion and PLR Measured from *Gnat1*^{-/-}; *cl/cl* mice, Related to Figure 4

(A) To calculate the upconversion efficiency of pbUCNPs, pbUCNPs were spreaded evenly on the surface of a cover glass: 2.4 cm \times 2.4 cm. 980 nm light was applied from the top of the cover glass covering a 1.5 cm \times 1.5 cm area and the intensity of emission light from the other side of the cover glass was measured behind a combined filters (bandpass filter at 510 - 560 nm and short-pass filter cutoff at 805 nm). The numerical aperture of the sensor in the light intensity meter is 0.75, which collected a proximately 17% of the isotropically emitted photons from pbUCNPs.

(B) The upconversion relationship between NIR and visible light intensities. From a linear fit in the log-log scale, we extracted the power relation between up-converted 535-nm emissions and 980-nm excitation light to be 1.6.

(C) Light induced pupillary light reflex (PLR) dose response curves and their Hill function fitting (markers and solid lines) for visible (black) and NIR (red) light. The Hill coefficients for visible and NIR light PLR dose response are 0.78 and 1.10, respectively. To calculate the theoretical NIR light PLR dose response curve, NIR light intensities were applied to the upconversion relationship to generate upconverted corresponding visible light intensities, and then these intensities were

(legend continued on next page)

applied to visible light PLR dose response Hill function. The theoretical NIR light PLR dose response curve (red dashed line) matched very well to the experimental measurement. Therefore, the non-linearity shown in the light induced behavior is attributed to the non-linearity of the upconversion process.

(D) Spectrum of 980-nm LED light in log scale. Inset: expanded view of this spectrum in linear scale.

(E) Expanded view of (D) at above 900 nm in log scale.

(F) PLR from *Gnat1*^{-/-}; *cl/cl* mice, which have intrinsically photosensitive retinal ganglion cells (ipRGCs) as the only functional photoreceptors. All data are mean \pm SD.

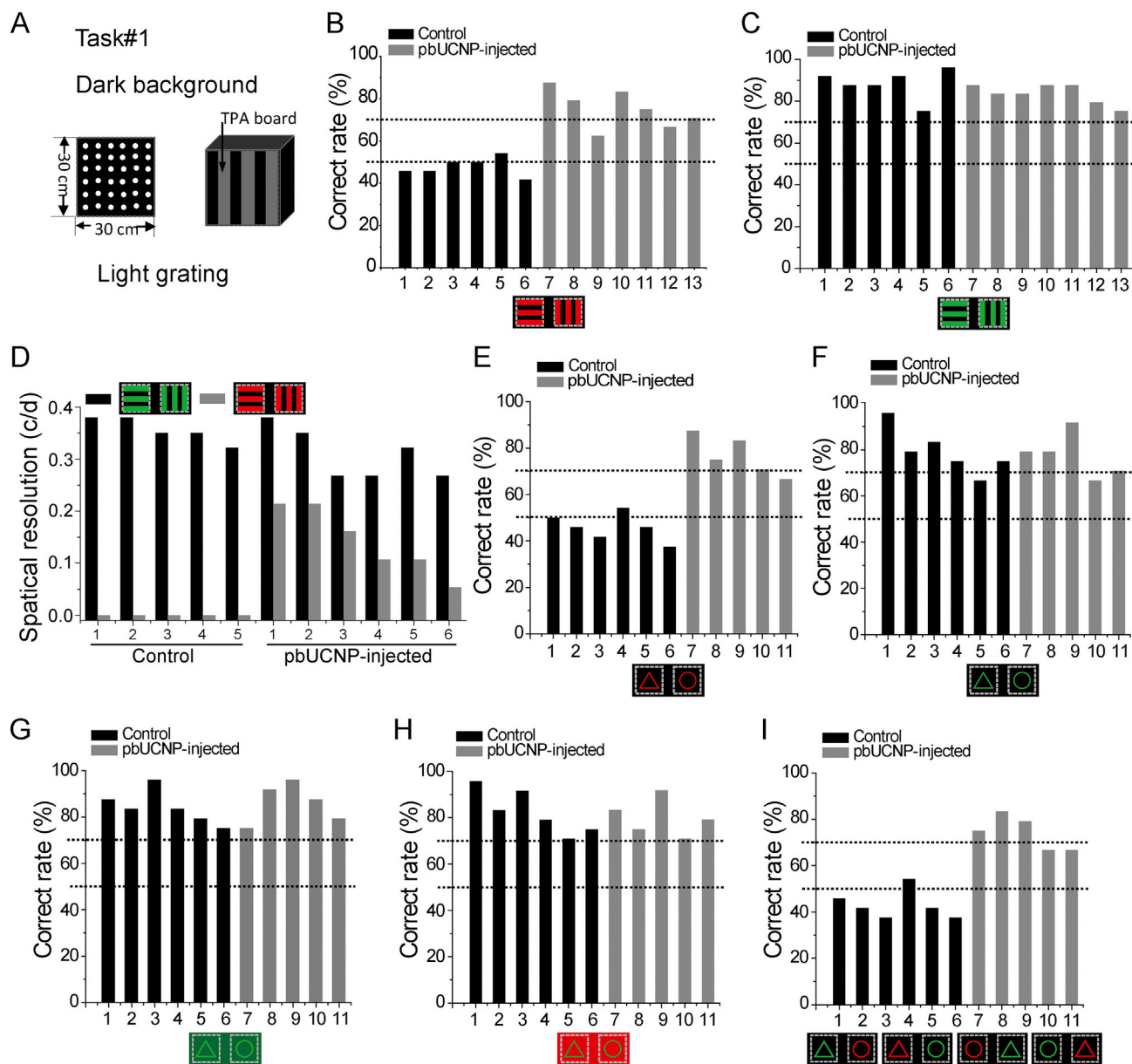


Figure S6. Simultaneous NIR and Visible Light Pattern Vision, Related to Figure 6

- (A) Diagram of the light grating stimuli made from LED arrays and transparent acrylic (TPA) boards.
- (B) Correct rates made by each individual animal in discriminating NIR light gratings.
- (C) Correct rates made by each individual animal in discriminating visible light gratings.
- (D) The visual imaging resolution for each individual animal for visible (dark) and NIR (gray) light gratings.
- (E) Correct rates made by each individual animal in discriminating NIR light triangle and circle under dark background.
- (F) Correct rates made by each individual animal in discriminating visible light triangle and circle under dark background.
- (G) Correct rates made by each individual animal in discriminating visible light triangle and circle under visible light background.
- (H) Correct rates made by each individual animal in discriminating visible light triangle and circle under NIR light background.
- (I) Correct rates made by each individual animal in discriminating NIR and visible light triangle and circle simultaneously.